J. Fluid Mech. (2003), *vol.* 488, *pp.* 79–121.
DOI: 10.1017/S0022112003004798 Printed in the United Kingdom

Receptivity of a supersonic boundary layer over a flat plate. Part 2. Receptivity to free-stream sound

By YANBAO MA AND XIAOLIN ZHONG

Mechanical and Aerospace Engineering Department, University of California, Los Angeles, CA 90095, USA

(Received 23 April 2002 and in revised form 28 February 2003)

In this paper, we continue to study the mechanisms of the receptivity of the supersonic boundary layer to free-stream disturbances by using both direct numerical simulation and linear stability theory. Specifically, the receptivity of a Mach 4.5 flow over a flat plate to free-stream fast acoustic waves is studied. The receptivity to free-stream slow acoustic waves, entropy waves and vorticity waves will be studied in the future. The oblique shock wave induced by the boundary-layer displacement plays an important role in the receptivity because the free-stream disturbance waves first pass through the shock before entering the boundary layer. A high-order shock-fitting scheme is used in the numerical simulations in order to account for the effects of interactions between free-stream disturbance waves and the oblique shock wave. The results show that the receptivity of the flat-plate boundary layer to free-stream fast acoustic waves leads to the excitation of both Mack modes and a family of stable modes, i.e. mode I, mode II, etc. It is found that the forcing fast acoustic waves do not interact directly with the unstable Mack modes. Instead, the stable mode I waves play an important role in the receptivity process because they interact with both the forcing acoustic waves and the unstable Mack-mode waves. Through the interactions, the stable mode I waves transfer wave energy from the forcing fast acoustic waves to the second Mack-mode waves. The effects of incident wave angles, forcing wave frequencies, and wall temperature perturbation conditions on the receptivity are studied. The results show that the receptivity mechanisms of the second mode are very different from those of modes I and II, which leads to very different receptivity properties of these discrete wave modes to free-stream fast acoustic waves with different incident wave angles, frequencies, and different wall boundary conditions. The maximum receptivities of the second mode, mode I and mode II to planar free-stream fast acoustic waves are obtained when incident wave angles approximately equal 26°, 45°, and 18°, respectively. The results of receptivity to a beam of free-stream fast acoustic waves show that the leading edge is one of the most efficient regions for receptivity.

1. Introduction

The study of laminar–turbulent transition in supersonic and hypersonic boundary layers is important to the development of future space vehicles operating at sustained supersonic and hypersonic speeds. In an environment with small initial disturbances, the paths to transition can conceptually be divided into three stages: (i) receptivity, (ii) linear eigenmode growth or transient growth, and (iii) nonlinear breakdown to turbulence. The first stage is the receptivity process, which converts the environmental

disturbances into instability waves, such as the Tollmien–Schlichting (T-S) waves, in the boundary layers. The study of the receptivity mechanisms is important because it provides important initial conditions of amplitude, frequency, and phase angles for the instability waves in the boundary layers (Goldstein & Hultgren 1989). The main objective of a receptivity study of a boundary layer is to investigate the properties and mechanisms of initial generation of unstable boundary-layer wave modes by forcing waves.

This paper is concerned with the receptivity of a supersonic boundary layer over a flat plate. The unstable wave modes in a supersonic boundary layer have been identified and extensively studied by Mack (1984) using the linear stability theory (LST). Mack found that, in a supersonic or hypersonic boundary layer, there are multiple higher instability modes in addition to the first instability mode, which is the compressible counterpart of T-S waves in incompressible boundary layers. The instability modes in supersonic boundary layers, i.e. the first mode, the second mode, the third mode, etc., have been termed the Mack modes. Among them, the second mode is most important and has been extensively studied because it becomes the dominant boundary-layer unstable mode in supersonic boundary layers at Mach numbers larger than about 4. On the other hand, the oblique first mode is most unstable for supersonic flow at lower Mach numbers. Therefore, the receptivities of the first and the second modes to forcing disturbances are the main goal of a receptivity study of a supersonic boundary layer.

Though the linear stability properties of the unstable Mack modes in supersonic boundary layers are well understood, it is still a subject of current research with regard to the receptivity of the supersonic boundary layers, i.e. the generation mechanisms of the unstable Mack modes by various forcing waves. There have been a number of experimental studies on the receptivity of supersonic and hypersonic boundary layers (Maslov & Semionov 1986; Semionov, Kosinpv & Maslov 1996, 1998; Arnal *et al.* 1999; Maslov *et al.* 2001). It was found that the forcing fast acoustic waves impinging on the leading edge generate Tollmien–Schlichting waves in supersonic boundary layers. There is a dependence of receptivity coefficients on the incident wave angles of the forcing waves. On the other hand, most of the computational and theoretical studies on boundary-layer receptivity have been mostly for incompressible flow, which have been reviewed by Saric Reed & Kerschen (2002). There have been only a few theoretical and computational studies on the receptivity of compressible boundary layers (Mack 1975; Gaponov 1977; Kerschen 1989; Choudhari & Streett 1990, 1993; Fedorov & Khokhlov 1991, 1992). Fedorov and colleagues (Fedorov & Alexander 1997; Fedorov & Khokhlov 2001, 2002; Fedorov & Tumin 2001) showed by analysis that strong excitation occurs when external waves and wall induced disturbances are in resonance with the boundary-layer normal modes. Boundary-layer self-similar solutions were used in Fedorov's analyses. The effect of the bow shock wave on the receptivity process, however, was not considered. Zhong (2001) studied the receptivity of hypersonic flow over a parabola by numerical simulations of the full Navier–Stokes equations. The effects of bow shock and the entropy layer were accurately taken into account by using a fifth-order shock-fitting scheme. It was concluded that the generation of boundary-layer stability waves was mainly due to the interaction of the boundary layer with the transmitted fast acoustic waves instead of entropy and vorticity waves. The receptivity coefficient was found to increase as the relative nose radius was decreased. Malik, Lin & Sengupta (1999) studied the receptivity of Mach 8 flow past a sharp wedge with 5.3° half-angle to three different types of external disturbance by solving compressible linearized Navier–Stokes equations. The

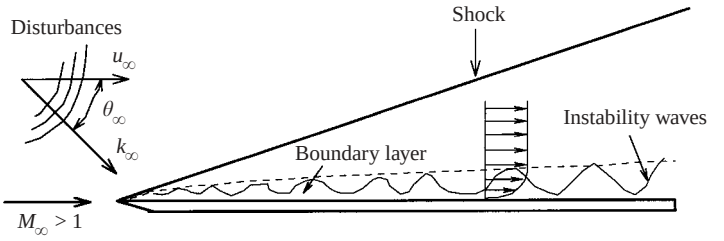

FIGURE 1. A diagram of the receptivity to free-stream disturbances for a supersonic boundary layer over a flat plate.

forcing disturbances include a surface suction/blowing embedded in a wedge surface, a narrow beam of free-stream fast acoustic waves, and planar free-stream fast acoustic waves. Their results showed that similar boundary-layer instability wave patterns are formed in all cases of different forcing disturbances. No quantitative analysis of the supersonic boundary-layer receptivity mechanism was done on the computational results.

Figure 1 shows a diagram of the receptivity process of a supersonic flat-plate boundary layer to free-stream disturbances. An oblique bow shock wave is generated in supersonic viscous flow over a flat plate owing to the displacement of the boundary layer by the viscous effects. The strength of the bow shock, which is not known in advance, depends on the free-stream Mach number and Reynolds number of the flow. The induced oblique shocks were neglected in most of the previous theoretical and computational studies of the stability and receptivity of supersonic and hypersonic boundary layers. Such simplification is acceptable in the linear stability theory (Mack 1984) because the stand-off distance of the shock away from the wall is relatively large compared with the boundary-layer thickness. Therefore, in linear stability analysis, the shock does not interact with the instability wave in the boundary layer. For the study of the supersonic boundary-layer receptivity to free-stream disturbances, however, the effects of the oblique shock on the receptivity can be significant, hence cannot be neglected. The receptivity phenomena can be altered considerably by the oblique shock over the boundary layers. In the receptivity process, the forcing free-stream disturbance waves must pass through the oblique shock wave before they enter the boundary layer to excite the unstable Mack modes. The interactions between the shock wave and the forcing waves generate complex wave patterns behind the shock. Therefore, it is necessary to include the shock interaction in numerical simulations of supersonic boundary-layer receptivity.

Kovasznay (1953) showed that weak disturbances in compressible flow can be decomposed into three kinds of independent wave mode: acoustic, entropy and vorticity waves. The acoustic waves propagate with the speed of sound relative to the moving fluid, whereas the entropy and vorticity waves convect with the moving fluid velocity. Before entering the boundary layer, free-stream disturbances pass through and interact with the shock. Irrespective of the nature of free-stream disturbance waves, it was shown that their interactions with the shock always generate all three kinds of wave behind the shock (McKenzie & Westphal 1968). These three kinds of transmitted wave propagate downstream and interact with the boundary layer on the flat plate. Meanwhile, the perturbed boundary layer also generates reflected acoustic waves propagating back to the shock. When the reflected acoustic waves reach the shock, they generate additional disturbances of all three kinds of wave which also

propagate downstream. The combined effects of these interactions between the oblique shock and forced free-stream disturbances as well as reflected acoustic waves from the wall can have strong effects on the receptivity process of the supersonic and hypersonic boundary layer behind the shock.

This paper is Part 2 of our study on the receptivity of a supersonic boundary layer over a flat plate. In Part 1 (Ma & Zhong 2003), the stability characteristics of the boundary-layer wave modes and their mutual resonant interactions were studied by using both direct numerical simulation (DNS) and linear stability analysis. It was found that, in addition to the conventional unstable first and second Mack modes, there exists a family of stable wave modes in the supersonic boundary layer. These stable modes were termed mode I, mode II, etc. in Ma & Zhong (2002). It was shown that although mode I and mode II waves are predicted to be stable by the linear stability theory, they can have resonant interactions with both acoustic waves and the Mack-mode waves. In addition, the stable wave modes such as mode I waves can transfer wave energy from the fast acoustic waves to the unsteady second-mode waves. Therefore, it is reasonable to expect that such stable mode waves can play a very important role in the excitation of the unstable Mack modes, especially the second mode, during the receptivity process to the free-stream fast acoustic waves. It was also found that the wavenumbers and wave mode structures predicted by the linear stability analysis agree very well with those obtained by the numerical simulations. However, the linear stability analysis consistently underpredicts the growth rates of all wave modes, including the Mack modes, because the non-parallel effects are neglected by the linear stability analysis. It is necessary to conduct an in-depth study on the receptivity process of the supersonic boundary layer to free-stream fast acoustic waves by using accurate numerical simulations.

The objective of this paper is to study the receptivity mechanisms of the supersonic boundary layer to free-stream fast acoustic waves by numerical simulations. The transient interactions of the forcing free-stream disturbance waves with the oblique bow shock are accurately taken into account in the numerical simulations by the high-order shock-fitting scheme used in Zhong (1998). In the simulations, the free-stream fast acoustic waves are superimposed on the steady base flow to investigate the generation of boundary-layer instability waves. The receptivity properties are analysed based on numerical simulations and by the linear stability analyses. The effects of forcing incident wave angles, forcing wave frequencies and wall temperature perturbations on the receptivity are studied. The numerical accuracy of the computational results for the present study is evaluated by grid refinement studies and by comparison with available theoretical results.

2. Governing equations and numerical methods

The governing equations, numerical methods, and flow parameters are described briefly in this section. Under a thermally and calorically perfect gas regime, the two-dimensional Navier–Stokes equations in conservative form can be written as:

$$\frac{\partial \boldsymbol{U}^*}{\partial t^*} + \frac{\partial}{\partial x^*}(\boldsymbol{F}_1^* + \boldsymbol{F}_{v1}^*) + \frac{\partial}{\partial y^*}(\boldsymbol{F}_2^* + \boldsymbol{F}_{v2}^*) = 0, \tag{1}$$

where the superscript '$*$' represents dimensional variables, and $\boldsymbol{U}^*$ is a vector containing the conservative variables, $\{\rho^*, \rho^* u^*, \rho^* v^*, e^*\}$. $\boldsymbol{F}_1^*$ and $\boldsymbol{F}_2^*$ are inviscid flux vectors and described in detail in Part 1 (Ma & Zhong 2003). Unless stated otherwise, dimensional flow variables in this paper are non-dimensionalized by using the

steady-state free-stream conditions. Specifically, velocities are non-dimensionalized by the free-stream velocity u^*_∞, length scales by a boundary-layer thickness length $L^* = x^*/R$, density by ρ^*_∞, pressure by p^*_∞, temperature by T^*_∞, time by L^*/u^*_∞, vorticity by u^*_∞/L^*, entropy by c^*_p, wavenumber by $1/L^*$, circular frequency by u^*_∞/L^*, etc. The dimensionless flow variables have the same notation as their dimensional counterparts, but without the superscript asterisk.

A fifth-order shock-fitting method of Zhong (1998) is used to compute the two-dimensional Navier–Stokes equations in the flow field bounded by the bow shock and the flat plate (figure 1). The shock-fitting method treats the bow shock as a computational boundary. The flow variables behind the shock are determined by Rankine–Hugoniot relations across the shock and a characteristic compatibility equation from behind the shock. The transient movement of the shock and its interaction with free-stream disturbance waves are solved as part of the solutions. The use of the shock-fitting method makes it possible to use high-order finite-difference schemes for spatial discretization. A fifth-order upwind finite-difference scheme is applied for the convective terms while a sixth-order central scheme is used for the discretization of the viscous terms. The spatial discretization of the governing equations leads to a system of first-order ordinary differential equations. An explicit Runge–Kutta method is used for temporal discretization. The details of the numerical method are in Zhong (1998) and are not repeated here.

As described in Part 1, the results computed by the second-order total variation diminishing (TVD) shock-capturing methods are used as inflow condition. The non-slip wall boundary condition is used for velocity. An adiabatic wall boundary condition is used for the steady base flow. For unsteady simulations, although it is more physical to assume isothermal wall ($T' = 0$) conditions other than adiabatic wall ($\partial T'/\partial y = 0$) for unsteady supersonic flow at high frequencies (Mack 1984; Malik 1990), both the adiabatic wall and isothermal wall boundary conditions are used for the temperature perturbations as two bounds for real cases if the physical condition for temperature perturbations is difficult to determine. In addition, the study of the effect of the two wall temperature boundary conditions on the boundary-layer receptivity helps to understand the receptivity process, which is shown in § 5. Although adiabatic wall and isothermal wall boundary conditions are commonly used for the base steady flow, $\partial T'/\partial y|_{y=0} = 0$ is called adiabatic wall and $T'|_{y=0} = 0$ is called isothermal wall for convenience of discussion in this paper without causing confusion.

3. Flow conditions

The same flow conditions as those in Part 1 are used to study the receptivity of a Mach 4.5 boundary-layer flow to free-stream sound because the stability of this Mach 4.5 flow has been extensively studied (Guo, Kleiser & Adams 1996; Kendall 1967; Kerschen 1989; Bayliss, Maestrello & Krishnan 1991; Pruett & Chang 1993). The flow conditions are also the same as those used in Kendall's (1975) experiment on the stability of a Mach 4.5 flow over a flat plate, i.e.

$$M_\infty = 4.5\,, \qquad T^*_\infty = 65.15\ \text{K},$$
$$p^*_\infty = 728.44\ \text{Pa}\,, \qquad Pr = 0.72,$$
$$\text{Unit Reynolds number: } Re^*_\infty = \frac{\rho^*_\infty u^*_\infty}{\mu^*_\infty} = 7.2 \times 10^6\ \text{m}^{-1}.$$

In many figures of this paper, the results are plotted as a function of the dimensional x^* coordinate along the flat plate because this case has been studied in previous

experiments. The dimensional x^* coordinate can be converted easily to dimensionless local Reynolds numbers according to the following formula:

$$Re_x = Re^*_\infty \, x^* = 7.2 \times 10^6 \, \mathrm{m}^{-1} x^*, \tag{2}$$

where x^* is the dimensional coordinate in metres measured from the leading edge along the plate surface for the current simulations. The range of computational domain and grid distribution of the current simulations have been presented in Part 1.

4. Free-stream disturbances

The receptivity of the supersonic boundary layer to free-stream disturbance waves is considered by the numerical simulations. The oblique shock plays an important role in the current study because the disturbance waves first pass through the shock before entering the boundary layer. In the simulations, the free-stream disturbances are superimposed on the steady base flow to investigate the excitation and the development of boundary-layer instability waves. The free-stream disturbances are assumed to be weak monochromatic planar fast acoustic waves before reaching the shock. The perturbations of flow variables in the free-stream introduced by the free-stream fast acoustic waves can be written in the following form:

$$\begin{Bmatrix} u' \\ v' \\ p' \\ \rho' \end{Bmatrix}_\infty = \begin{Bmatrix} |u'| \\ |v'| \\ |p'| \\ |\rho'| \end{Bmatrix}_\infty \exp[\mathrm{i}(k_x \, x + k_y \, y - \omega t)], \tag{3}$$

where $|u'|$, $|v'|$, $|p'|$ and $|\rho'|$ are dimensionless perturbation amplitudes satisfying the following relations:

$$|u'|_\infty = \epsilon k_x / k_\infty, \qquad |v'|_\infty = \epsilon k_y / k_\infty, \tag{4}$$

$$|p'|_\infty = \gamma M_\infty |u'|, \quad |\rho'|_\infty = |p'|/\gamma, \tag{5}$$

where ϵ is a small non-dimensional parameter representing the free-stream wave magnitude. The parameter k_∞ is the free-stream wavenumber with components k_x and k_y in the streamwise and wall-normal directions respectively, i.e.

$$k_x = k_\infty \cos(\theta_\infty), \qquad k_y = -k_\infty \sin(\theta_\infty), \tag{6}$$

where θ_∞ is the incident wave angle of the free-stream fast acoustic waves relative to the streamwise direction, as shown in figure 1. The non-dimensional wavenumber is related to the circular frequency ω by the dispersion relation:

$$\omega = k_\infty \, (1/M_\infty + \cos\theta_\infty). \tag{7}$$

The frequency is characterized by a dimensionless frequency F defined by

$$F = \frac{\omega^* \mu^*_\infty}{\rho^*_\infty u^{*2}_\infty}, \tag{8}$$

where ω^* is the dimensional circular frequency. The relation between non-dimensional circular frequency ω and F is

$$F = \frac{\omega}{R}. \tag{9}$$

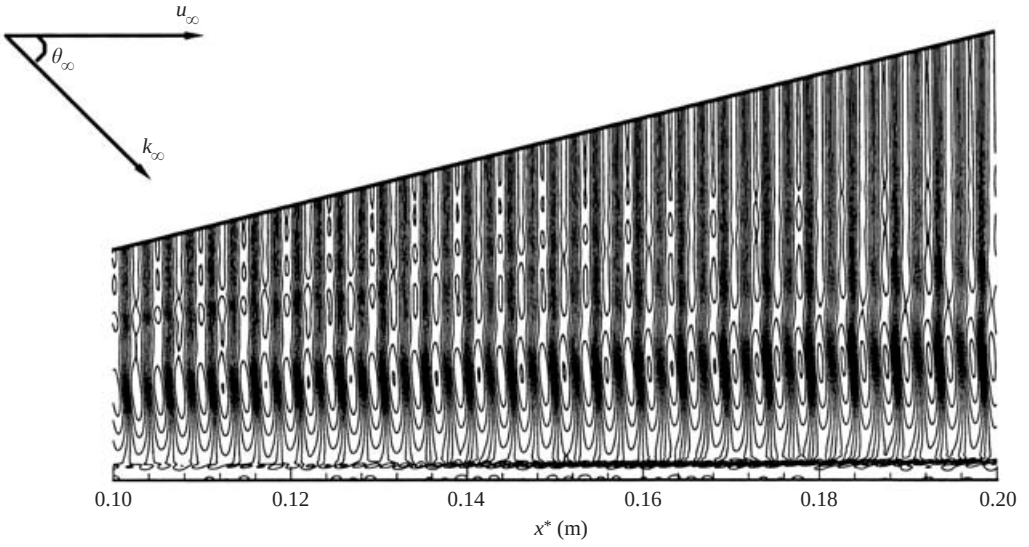

FIGURE 2. Instantaneous density perturbation contours induced by planar free-stream fast acoustic wave ($F = 2.2 \times 10^{-4}$ and $\theta_\infty = 0°$).

5. Receptivity to planar free-stream fast acoustic waves

In this group of cases, planar free-stream fast acoustic waves with different frequencies and incident wave angles (θ_∞) are imposed at the top of the computational boundary in front of the shock. The amplitude of the velocity disturbance in the freestream is chosen to be $\epsilon = 5.0 \times 10^{-4}$ so that the boundary-layer responses to the free-stream forcing waves are linear, which is demonstrated in our numerical tests. The receptivity mechanisms and properties of different boundary-layer discrete normal modes to planar free-stream fast acoustic waves with different incident wave angles, frequencies, and different wall boundary conditions are studied in this section.

5.1. *Distribution of disturbances in the flow field*

As in the first case, planar free-stream fast acoustic waves at $F = 2.2 \times 10^{-4}$ with zero incident angle ($\theta_\infty = 0$) are considered. Figure 2 shows the contours of instantaneous density perturbations induced by planar free-stream fast acoustic waves with zero incident wave angle. The upper boundary of the flow field stands for the position of the oblique shock wave. There are strong transmitted acoustic waves propagating in the direction almost parallel to the wall surface. Figure 2 also shows a typical rope-like second mode pattern near the wall in the region ($0.1\,\text{m} < x^* < 0.2\,\text{m}$), where the second mode is expected to be dominant based on our previous study (figure 16 in Part 1).

The distributions of the amplitudes of pressure disturbances along different streamwise grid lines are shown in figure 3, where $j = 1$ stands for the grid line on the wall surface, $j = 121$ represents the grid line immediately behind the shock, and $j = 41$, $j = 81$ are grid lines located in the middle of the flow field. The particular grid lines are also plotted in the figure to show their locations. This figure shows that the amplitudes of pressure perturbations change dramatically along different grid lines. Along the wall surface ($j = 1$), a complex wave structure for pressure disturbances is shown in this figure. Such a wave structure is the result of the excitation of several boundary-layer wave modes. The identification of different

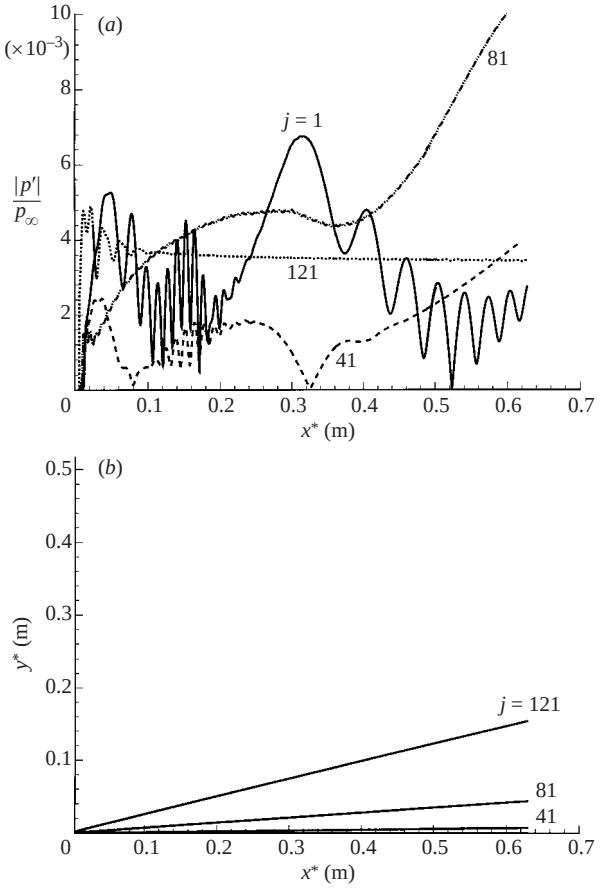

FIGURE 3. Distribution of (a) pressure perturbation along (b) different grid lines due to free-stream planar acoustic waves ($M_\infty = 4.5$, $Re_x = 7.2 \times 10^6\,\mathrm{m}^{-1}x^*$, $F = 2.2 \times 10^{-4}$ and $\theta_\infty = 0°$).

generated boundary-layer wave modes will be analysed in detail in this section. The maximum pressure perturbations occur outside the boundary layer owing to the interaction between transmitted acoustic waves behind the shock and reflected acoustic waves from the wall. This figure also shows that the amplitudes of pressure perturbations immediately behind the shock ($j = 121$) are almost constant in the downstream area. The interaction between free-stream disturbances and the shock wave is discussed below.

5.2. *Interaction between free-stream disturbances and the shock wave*

Again, the first case of a planar free-stream fast acoustic wave with zero angle ($\theta_\infty = 0$) is considered. Before entering the boundary layer, fast acoustic waves are first processed by the shock wave. The interaction between free-stream disturbances and the oblique shock generates all three kinds of disturbance waves, i.e. acoustic waves, vorticity waves and entropy waves, irrespective of the nature of the free-stream disturbance waves. The linear interaction between free-stream disturbance waves with an oblique shock was studied by McKenzie & Westphal (1968), among others. For a given shock angle, which is numerically computed for the current case as shown in figure 2, and given amplitude and incident wave angle of the free-stream fast

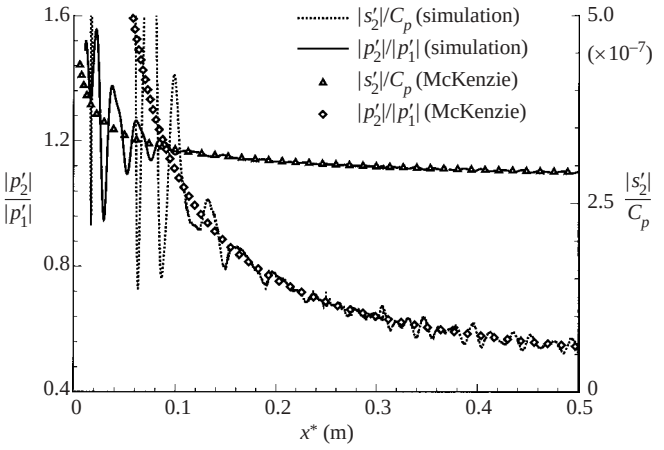

FIGURE 4. The distribution of the amplitudes of pressure and entropy perturbations immediately behind the oblique shock. The simulation results are compared with the linear theoretical results of McKenzie & Westphal (1968) ($F = 2.2 \times 10^{-4}$ and $\theta_\infty = 0°$).

acoustic waves, the amplitudes and wave angles of three generated disturbance waves immediately behind the oblique shock can be calculated from McKenzie & Westphal's theory. The theoretical results are valid under the condition that no wave or a very weak wave is reflected back to the shock from the boundary layer. Therefore, for the case of weak wave reflection towards the shock, theoretical predictions on wave transmission through the oblique shock can be used to validate the accuracy of the numerical simulations in computing the shock interactions.

Figure 4 compares amplitudes of pressure and entropy perturbations immediately behind the oblique shock between the numerical results and the theoretical results according to McKenzie & Westphal's theory. In the figure, subscripts 1 and 2 stand for the parameters in front of the shock and immediately behind the shock, respectively. There are strong oscillations on the numerical results of disturbance amplitudes near the leading edge. The reason for strong oscillations is because there are strong wave reflections between the shock and the boundary layer near the leading edge, where the shock is very close to the wall. As a result, the reflected disturbances from the wall interact with the shock wave to produce new waves behind the shock. The theoretical prediction is not expected to agree with the simulation in this region because the effect of wave reflection from the wall was not considered in Mckenzie & Westphal's theory. In the downstream region, on the other hand, the shock moves far away from the wall. The figure shows that, as expected, there is good agreement between the numerical results and theoretical predictions for both pressure and entropy disturbances downstream of the leading-edge region. The figure also shows that pressure disturbances are amplified owing to the interaction between free-stream fast acoustic waves and oblique shock. In addition, from Mckenzie & Westphal's linear theory, the maximum wave angle (relative to the horizontal direction) of the transmitted fast acoustic waves is less than 1.02° for the current case. Therefore, the transmitted acoustic waves propagate in the direction almost parallel to the wall surface shown in figure 2.

The shock oscillations induced by the planar free-stream fast acoustic waves are shown in figure 5. The shock oscillations are normalized by the fast acoustic

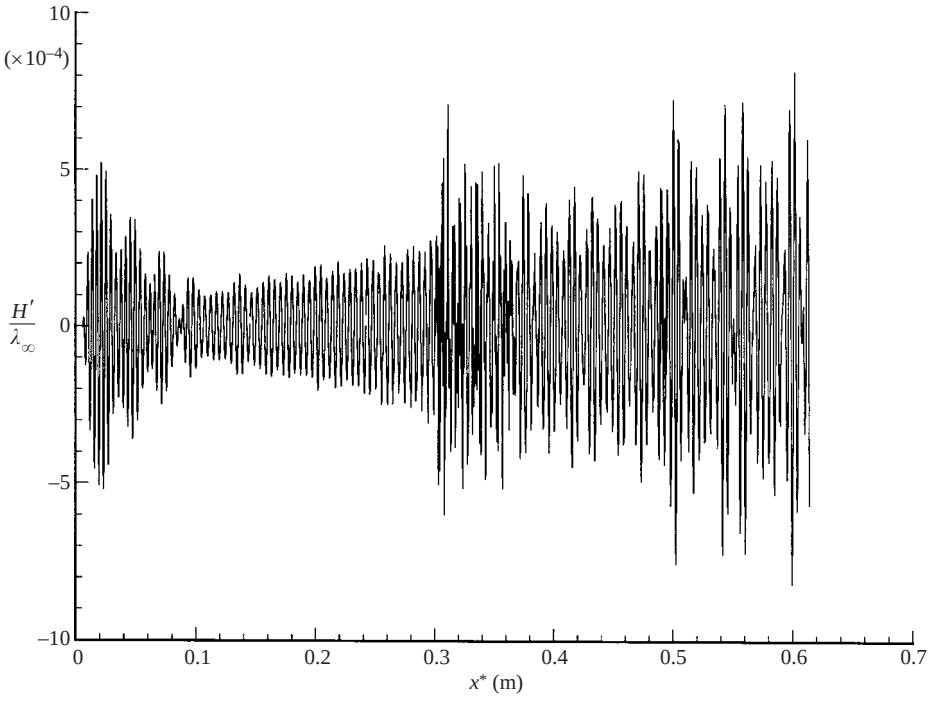

FIGURE 5. Instantaneous shock perturbations induced by a planar acoustic wave from the free stream ($F = 2.2 \times 10^{-4}$ and $\theta_\infty = 0°$).

wavelength in the free stream. The figure shows that the amplitudes of shock oscillations are less than 0.1% of the acoustic wavelength.

5.3. *Identification of boundary-layer wave modes*

Figure 6 shows the distribution of instantaneous pressure perturbations along the wall surface. Pressure perturbations on the wall show complex wave patterns, which indicates the existence of a number of wave modes generated in the boundary layer by the receptivity process. The discrete wave modes induced in the boundary layer include both Mack modes and a family of stable modes, such as mode I, mode II, etc. Based on our previous study (figure 16 in Part 1), the second Mack-mode disturbances are expected to be the dominant instability waves in a local region between $x^* = 0.1$ m ($R = 848.5$) and $x^* = 0.2$ m ($R = 1200$). However, figure 6 shows that there are no dominant second-mode disturbances in this range. On the contrary, a clearly dominant wave mode appears after $x^* = 0.2$ m. Its amplitudes increase before reaching a peak value at $x^* \approx 0.31$ m, although all normal modes are stable in this region as predicted by the linear stability theory. In fact, a strongly unstable band lying at frequencies beyond the second-mode one was also observed in Kendall's (1975) experiment on hypersonic boundary-layer disturbances induced by acoustic waves. So far, the contradiction on the stability of the boundary-layer normal mode between experimental observation and the LST results has not been resolved. Therefore, it is necessary to identify all the different wave modes in the boundary layer in order to understand the receptivity mechanisms.

As the first step, the dominant wave mode in the downstream region is identified. The change of pressure perturbations along the wall surface in the downstream region shown in figure 6 has very similar wave patterns as those of mode II when a single

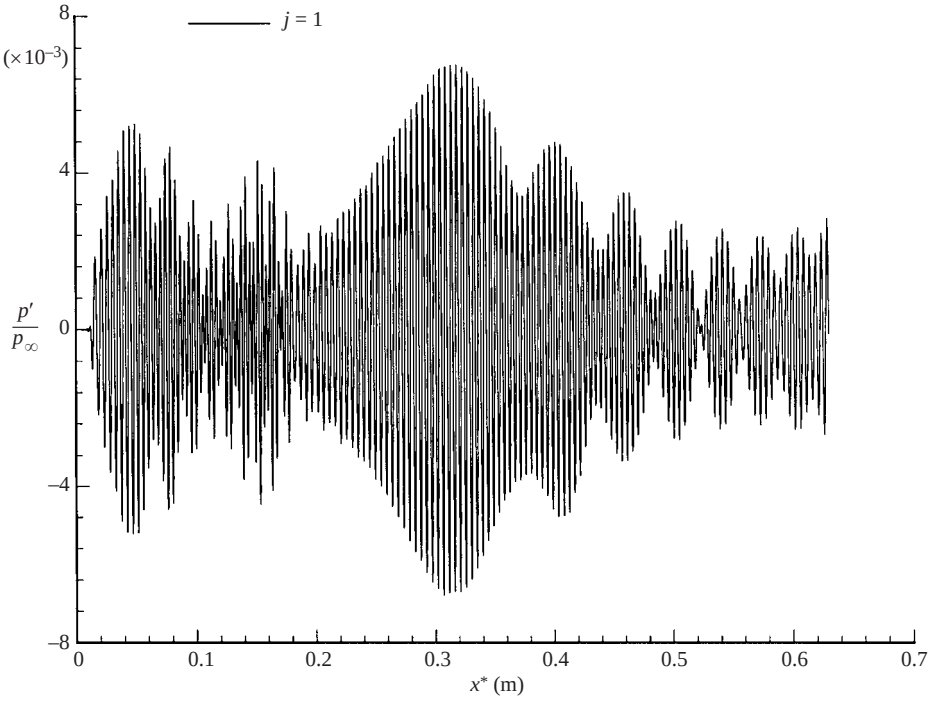

FIGURE 6. Instantaneous pressure perturbations along the wall surface for the case of a planar acoustic forcing wave from the free stream ($F = 2.2 \times 10^{-4}$ and $\theta_\infty = 0°$).

mode II wave is introduced at the inlet (see figure 28 in Part 1). Though mode II is predicted to be always stable by the linear stability theory, it was shown that the growth of mode II is caused by a resonant interaction between mode II disturbances inside the boundary layer and fast acoustic waves outside the boundary layer in the region near the synchronization point between the two waves (Part 1). Figure 7 compares the amplitudes of pressure perturbations along the wall surface due to two different ways of imposing disturbances: the current case of planar free-stream fast acoustic waves and the previous case of imposing a mode II wave at the inlet located at $x^* = 0.185$ m (figure 28 in Part 1). The amplitudes of mode II waves which are introduced at the inlet are multiplied by a factor so that the maximum amplitude of pressure perturbations on the wall surface is the same as that induced by planar free-stream fast acoustic waves in the current case. This figure shows that there are very similar wave patterns of growth and decay for pressure perturbations in the two cases. Hence, the receptivity to the free-stream fast acoustic wave generates mode II waves in this region. To support this conclusion, figure 8 compares the profiles of induced disturbances with the structure of the mode II wave obtained from linear stability theory at $x^* = 0.362$ m ($R = 1614.43$). It shows that the structure of induced disturbances inside the boundary layer ($y^*/L^* < 12.9$) from the numerical simulations matches the structure of the mode II wave from linear stability theory very well. The differences in the region outside the boundary layer are due to the existence of transmitted acoustic waves outside the boundary layer in the numerical simulations. Therefore, the boundary-layer disturbances in the downstream region ($x^* > 0.2$ m) of current case contain a dominant mode II.

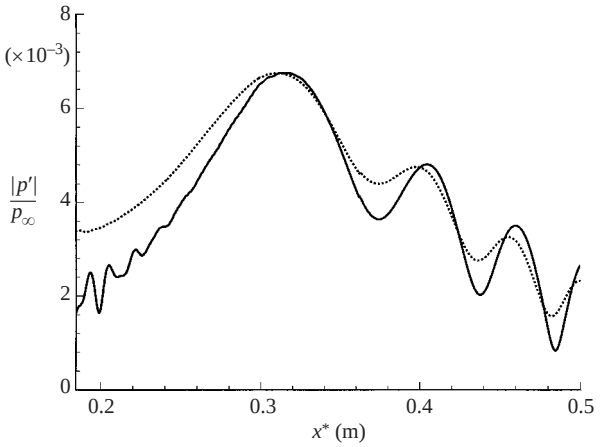

FIGURE 7. Comparison of amplitudes of pressure perturbations along the wall surface for two cases of different ways of imposing forcing perturbations ($F = 2.2 \times 10^{-4}$).. . . , mode II (forcing at the inlet); —, forcing from plane acoustic wave.

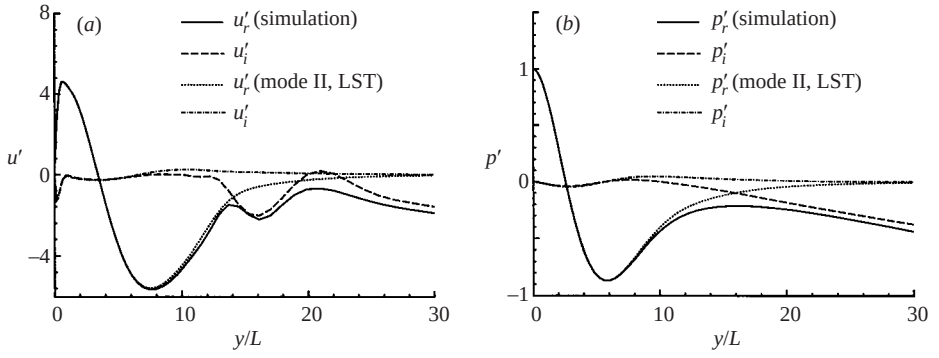

FIGURE 8. Comparison of the wave structures of disturbances induced by free-stream fast acoustic waves and those of mode II obtained by the linear stability theory at $R = 1614.43$ ($F = 2.2 \times 10^{-4}$ and $\theta_\infty = 0°$).

The phase velocities of the induced boundary-layer disturbances from numerical simulations are calculated based on pressure perturbations by using temporal Fourier analysis according to the following formula:

$$\alpha_r = \frac{\mathrm{d}\psi}{\mathrm{d}x}, \tag{10}$$

$$a = \frac{RF}{\alpha_r}, \tag{11}$$

where ψ is the phase angle from temporal Fourier analysis. The values calculated by using (10) and (11) correspond to the streamwise wavenumber (α_r) and phase velocity (a) of a single wave if the numerical solutions are dominated by a single discrete wave mode in a local region. If the numerical solutions contain a mixture of two or more wave modes, the values of the streamwise wavenumber and the phase velocity demonstrate the result of a modulation of these mixed wave modes. Figure 9 shows the distribution of the phase velocities along the wall surface. The phase velocities of the Mack modes, mode I and mode II from the linear stability theory are

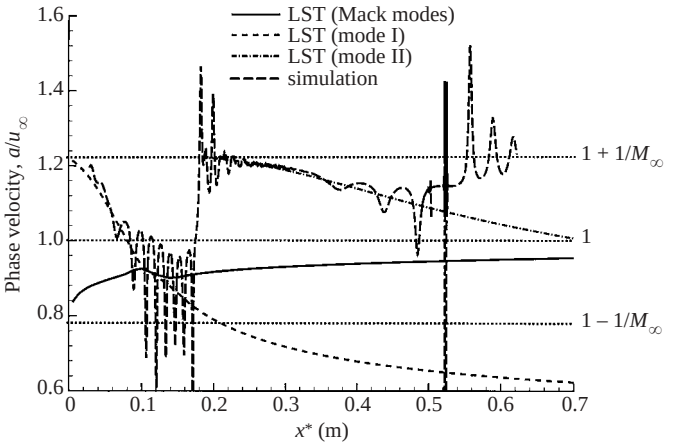

FIGURE 9. Distribution of phase velocity along the wall surface ($F = 2.2 \times 10^{-4}$ and $\theta_\infty = 0°$).

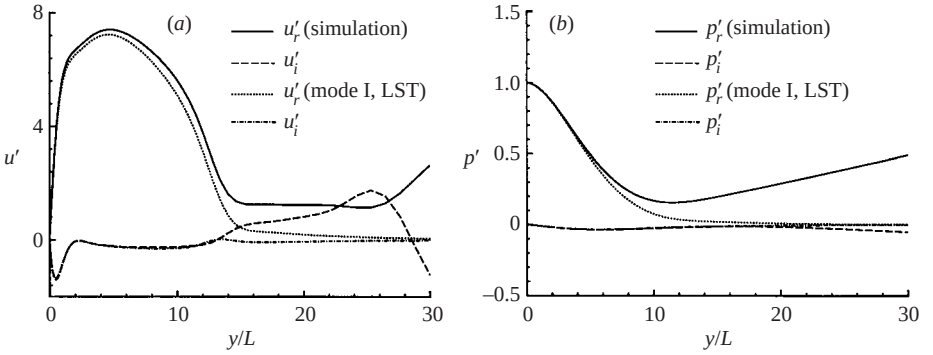

FIGURE 10. Comparison of the wave structures of disturbances induced by free-stream fast acoustic waves and those of mode I disturbances of linear stability theory at $R = 684.11$ ($F = 2.2 \times 10^{-4}$ and $\theta_\infty = 0°$).

also plotted in the same figure for comparison with the numerical solutions. In the figure, the long-dashed line represents the results of phase velocities from numerical simulations, while the solid line, the short-dashed line and the dash-dot line stand for phase velocities of the Mack modes, mode I and mode II from linear stability analysis, respectively. The figure shows that phase velocities of the induced waves are close to those of mode I waves in the upstream region ($x^* < 0.1$ m). This indicates that mode I waves are generated inside the boundary layer owing to the resonant interaction between mode I waves and fast acoustic waves near the leading edge. This is confirmed by the fact that the structures of the induced disturbances can match the structure of mode I from the linear stability theory in this region. Figure 10 compares the structure of disturbances induced by free-stream fast acoustic waves and the structure of mode I disturbances from linear stability theory at a grid station $x^* = 0.065$ m. Again, there is good agreement in the structure of disturbances between simulation results and LST results, except for the difference in the region outside the boundary layer owing to transmitted acoustic waves in the numerical simulations.

Figure 9 also shows that the phase velocities of mode I waves decrease during propagation downstream. As a result, mode I waves decay because of their inherent

stable properties when phase velocities of mode I waves decrease to a certain value and there is no more resonant interaction between mode I waves and acoustic waves after passing the first peak at $x^* = 0.0492$ m, which is shown in figure 6. Before mode I waves die out during propagation, they are synchronized with the Mack mode at $x^* = 0.11$ m. According to our previous study (figure 7 in Part 1), both the first Mack-mode waves and mode I waves have almost the same profiles of disturbance structure across the boundary layer at the synchronization point. As a result, mode I waves convert to the Mack-mode waves in the synchronization region (figure 9). figure 9 also shows a strong oscillation in the phase velocity plot between $x^* = 0.1$ m and $x^* = 0.2$ m, where the second mode is expected to be dominant. The oscillation in the phase velocity curve results from the modulation between the second-mode waves and other wave modes.

In the region further downstream ($x^* > 0.2$ m), figure 9 shows that the disturbances in the boundary layer are dominated by mode II. As shown in figure 8, the structures of induced disturbances match the structure of mode II predicted by the linear stability theory in this region. At location of $x^* > 0.5$ m, mode II waves die down because of their inherent stable properties. As a result, no dominant modes exist in this region. Therefore, there are strong oscillations in phase velocities again in the region even further downstream ($x^* > 0.5$ m).

Based on the preceding analysis, the induced wave structures demonstrated by the distribution of pressure perturbations and phase velocities along the wall can be summarized as follows. After the interaction between the free-stream fast acoustic waves and the oblique shock, the transmitted acoustic waves penetrate the boundary layer to form the Stokes waves which are the combination of acoustic waves, vorticity waves and entropy waves. Among the Stokes waves, the components of fast acoustic waves are dominant. The incident fast acoustic waves are reflected by the wall surface after the impingement on the wall. As a result, mode I disturbances are first generated because of the synchronization of wavenumbers or wave speeds between mode I waves and the fast acoustic waves near the leading edge. Though mode I is stable from the LST results, the amplitudes of induced mode I waves grow as they propagate downstream because there is strong resonant interaction between mode I waves and the acoustic waves in the region near the leading edge. After reaching the first peak value at $x^* = 0.0492$ m (figure 6), mode I waves decay because of their inherent stable properties after phase velocities of mode I waves decrease and there is no more resonance between mode I waves and acoustic waves. Before mode I waves die out during propagation, they are synchronized with the Mack mode. At the synchronization point, the phase velocity of the first mode is same as that of mode I. Furthermore, both the first Mack-mode waves and mode I waves have almost the same profiles of disturbance structure across the boundary layer at the synchronization point. As a result, mode I waves convert to the Mack-mode waves in the synchronization region (figure 9). Subsequently, the developed Mack-mode waves are amplified after they enter the second-mode unstable region. In this region, there exist second-mode waves and the Stokes waves (dominated by fast acoustic waves) as discussed above. The phase velocities of the second-mode waves are substantially different from those of the fast acoustic waves. Therefore, in this region ($0.1\text{ m} < x^* < 0.2$ m), there is wave modulation between the second-mode waves and the fast acoustic waves, which leads to a strong oscillation in the phase velocity curve between $x^* = 0.1$ m and $x^* = 0.2$ m as shown in figure 9. The second-mode waves decay after they pass the Branch II neutral point and become stable at $x^* = 0.155$ m. In the downstream region ($x^* > 0.2$ m), mode II waves are generated because of

the synchronization between mode II waves and fast acoustic waves. Because of the resonance between mode II waves and the acoustic waves, mode II waves are significantly amplified. In the region further downstream, mode II waves decay owing to their inherent stable property after their phase velocities decrease and there is no more resonance between mode II waves and the acoustic waves. The modulation between mode II waves and acoustic waves results in strong oscillation in pressure perturbations and phase velocities on the wall after $x^* > 0.34\,\mathrm{m}$.

Therefore, the stable mode I waves play an important role in the receptivity process. They exchange energy with both the forcing acoustic waves and Mack-mode waves. The Mack modes are converted from mode I waves in the boundary layer owing to the synchronization and energy exchange with mode I waves.

5.4. *Decomposition of boundary-layer wave modes*

In response to the forcing free-stream disturbance waves, a number of discrete wave modes as well as the Stokes waves with continuous spectra are generated in the boundary layer. These wave modes together with the forcing fast acoustic waves form the disturbance field obtained in the numerical simulation. To further analyse the receptivity of the boundary layer to the free-stream fast acoustic wave, it is necessary to decompose various wave modes induced in the boundary layer. By doing so, a receptivity coefficient, which is defined as the ratio of induced wave amplitude in the boundary layer to that of the forcing free-stream disturbance waves, can be determined.

In the current study, it is found that different discrete modes are generated and develop in different regions of the flow field in the receptivity to free-stream fast acoustic waves. For example, at $F = 2.2 \times 10^{-4}$, mode I waves exist in the region of $x^* < 0.1\,\mathrm{m}$, Mack-mode waves show up in the region of $0.1\,\mathrm{m} < x^* < 0.2\,\mathrm{m}$, and mode II waves are dominant in the region of $x^* > 0.2\,\mathrm{m}$. Meanwhile, the Stokes waves dominated by fast acoustic waves exist in the boundary layer of all different regions. As shown in figure 9, the Mack-mode waves and fast acoustic waves have very different wavenumbers. This can be used to extract wave components of the second Mack mode from the overall disturbance field in the boundary layer by means of a spatial Fourier analysis. Spatial Fourier analyses are performed in different zones of the computational domain as follows:

$$P(k) = \sum_{n=0}^{N-1} p(n) \exp(-j2\pi kn/N), \qquad k = 0, 1, 2, \ldots, N-1, \tag{12}$$

where $P(k)$ stands for the spectrum of spatial distribution of pressure at spatial frequency (wavenumber) $\omega_k = 2\pi k/(N\Delta x)$, $\Delta x = x_{n+1} - x_n$ and $N = 8192$. Here, zero padding is used when N is greater than the total number of available data points.

Figure 11 shows the spatial spectra (wavenumbers) of pressure disturbances on the wall in three continuous zones: zone 5, zone 6, zone 7, where the spatial intervals of zone 5, zone 6 and zone 7 are $0.105\,\mathrm{m} \leqslant x^* \leqslant 0.153\,\mathrm{m}$, $0.145\,\mathrm{m} \leqslant x^* \leqslant 0.193\,\mathrm{m}$ and $0.185\,\mathrm{m} \leqslant x^* \leqslant 0.25\,\mathrm{m}$, respectively. Figure 11 shows that there are two major peaks in pressure perturbations in zone 5 and zone 6, where the second-mode waves are expected to be dominant. The first peak has a wavenumber of $k^* \approx 1323.6\,\mathrm{m}^{-1}$ and the corresponding phase velocity is $a = 1.20$, which is very close to the phase velocity of the fast acoustic wave $1 + 1/M_\infty = 1.22$. The second peak has a wavenumber of $k^* \approx 1800\,\mathrm{m}^{-1}$ and the corresponding phase velocity is $a = 0.88$, which is very close to the phase velocity of the second Mack-mode waves at the Branch II neutral

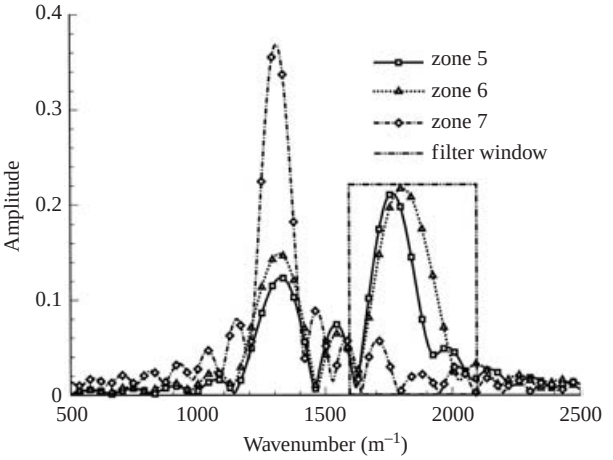

FIGURE 11. Amplitude of pressure perturbations in spatial wavenumber domain ($F = 2.2 \times 10^{-4}$ and $\theta_\infty = 0°$).

point ($RF = 0.2324$ and $a = 0.90$). In zone 7, the wavenumber spectra show only one dominant peak located at $k^* = 1307.9\,\mathrm{m}^{-1}$. The wave spectra shown in figure 11 are consistent with our analysis about different components included in boundary-layer disturbances. Both the second Mack-mode waves and fast acoustic waves exist in zone 5 and zone 6. Because Mack-mode waves and fast acoustic waves have very different wavenumbers, there are two peaks associated with these two different waves in the spectra of boundary-layer disturbances. Similarly, both mode II waves and fast acoustic waves coexist in zone 7. However, the phase velocities of mode II waves are very close to those of fast acoustic waves in this zone. Therefore, there is only one dominant peak when the computational zone is located downstream where $x^* > 0.2\,\mathrm{m}$.

Since there is a large difference in phase velocities (or wavenumbers) between the second-mode waves and the fast acoustic waves, these two different waves can be separated by a Fourier analysis. A band-pass filter window is put upon the second peak of wave spectra to extract the second-mode disturbances (see figure 11) by using the inverse discrete Fourier transform of $P(k)$,

$$p(n) = \sum_{n=0}^{N-1} P(k)W(k)\exp(j2\pi kn/N), \qquad n = 0, 1, 2, \ldots, N-1, \tag{13}$$

where $W(k) = 1$ when ω_k is located in the second-mode range, otherwise $W(k) = 0$. Figure 12 shows instantaneous pressure disturbances of the extracted second Mack mode induced by the planar acoustic waves. The growth and decay of the extracted second mode is very similar to the results shown in Part 1 (figure 16), where only a single Mack mode is introduced at the inlet. Figure 13 compares the second-mode wave structures separated from the numerical solutions by the Fourier analysis with those from the linear stability theory. The wave structures obtained by the numerical solutions before wave decomposition are also shown together for comparison. It shows that the unseparated waves contain a strong component of acoustic waves outside the boundary layer. The acoustic components are removed from the total boundary-layer disturbances by using the Fourier analysis. The separated second-mode wave structures agree well with those of the second mode predicted by the

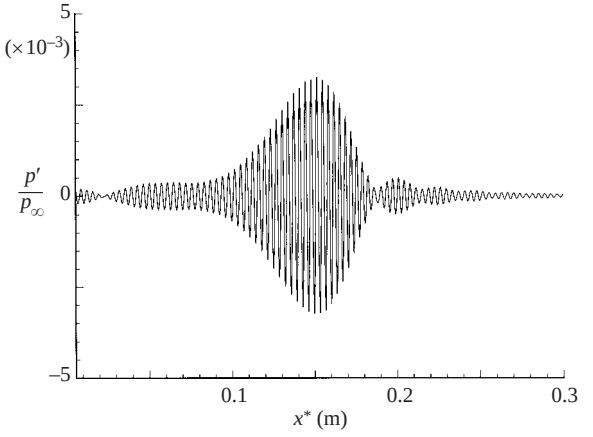

FIGURE 12. Distribution of the second-mode disturbances separated from the total boundary-layer disturbances induced by the free-stream fast acoustic wave ($F = 2.2 \times 10^{-4}$ and $\theta_\infty = 0°$).

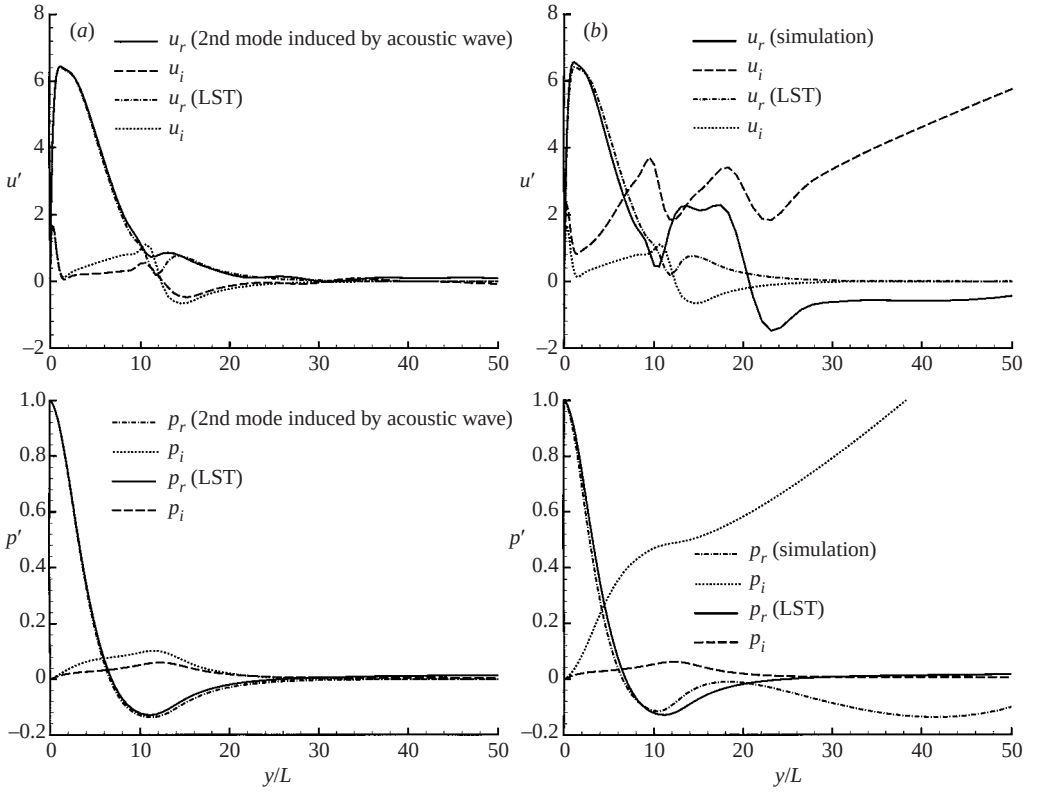

FIGURE 13. Comparison of (*a*) the wave structures of the separated second mode, (*b*) the unseparated simulation wave fields, and those obtained from linear stability theory for the second mode ($R = 1033$, $F = 2.2 \times 10^{-4}$ and $\theta_\infty = 0°$).

linear stability theory. Therefore, the extracted wave mode is indeed the second mode. The receptivity coefficient of the second mode can be computed based on the result of the extracted second mode from the numerical simulations.

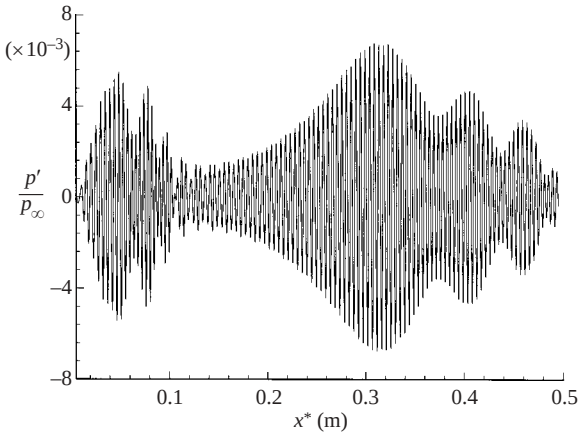

FIGURE 14. Instantaneous pressure perturbations along the wall surface after subtracting the second mode disturbances ($F = 2.2 \times 10^{-4}$ and $\theta_\infty = 0°$).

Figure 14 shows the wave components after the second Mack-mode waves have been removed. After removing the second-mode components, the envelope of disturbances becomes much smoother between $x^* = 0.1$ m and $x^* = 0.2$ m as compared to that shown in figure 6. The wave components shown in figure 14 consist of mode I waves, mode II waves and the Stokes waves. Unlike the case of the second mode, it is very difficult to decompose mode I and mode II from the total disturbances by using a band-pass filter window because the wave speeds of mode I (or mode II) are very close to those of the acoustic waves. On the other hand, the results shown in figure 9 indicate that at locations where mode I (or mode II) waves reach their maximum wave amplitudes, the wave components inside the boundary layer are dominantly the components for mode I (or mode II) only, which is proved by the comparison of mode I and mode II structures from the linear stability theory with the corresponding numerical solutions shown in figures 8 and 10. Therefore, even though a clean response coefficient for mode I and mode II cannot be obtained from the numerical solutions, an approximate value can be obtained by using the maximum wave amplitudes in the mode I and mode II region. Furthermore, the main interest of a receptivity study is on the response and receptivity coefficients of the unsteady second mode other than stable mode I and mode II. The response and receptivity coefficients for the second mode can be determined accurately from the numerical simulation results by spatial Fourier decompositions.

5.5. *Response coefficients*

We define a response coefficient to quantitatively study the acoustic receptivity of the boundary layer. Specifically, the response coefficient of the boundary layer to forcing disturbances for a given mode is defined as

$$K_{mode} = \frac{|p'_{mode}|}{|p'_\infty|}, \tag{14}$$

where $|p'|_{mode}$ is the maximum amplitude of pressure perturbations for the given wave mode. For the second mode, this maximum value is located at the Branch II neutral point of the decomposed second-mode waves as shown in figure 12. The response coefficients are used to measure the maximum responses of the relevant wave modes to forcing disturbances. Since they are not the same as the commonly used Branch I

receptivity coefficient used in the literature (Saric *et al.* 2002), they are termed the response coefficients in this paper. The Branch I receptivity coefficient for the second mode will be considered later in this section.

In the upstream region near the leading edge, the disturbance waves are dominated by mode I waves. The response coefficient for the mode I wave is close to the receptivity coefficient of mode I. In the downstream region, mode II waves are dominant. The response coefficient for the mode II wave in this region is close to the receptivity coefficient of mode II. On the other hand, boundary-layer disturbances in mode I and mode II dominant regions also contain some relatively weak Stokes waves, which cannot be separated from mode I and mode II waves. Therefore, we use the term response coefficient instead of receptivity coefficient for mode I and mode II waves. For example, for the current case of free-stream fast acoustic waves at zero incident wave angle, the response coefficients for the second mode, mode I and mode II are:

$$\begin{aligned} &\text{Second mode: } K_{second} = 1.03,\\ &\text{Mode I: } \quad K_{modeI} = 1.75,\\ &\text{Mode II: } \quad K_{modeII} = 2.14. \end{aligned}$$

Mode II has much stronger receptivity than the other two modes because of its resonant interaction with the fast acoustic waves.

5.6. *Effects of incident wave angles of the forcing waves*

The forcing fast acoustic waves in the free-stream can impinge on the flat plate at different incident wave angles. The effects of incident wave angles on the receptivity are studied by numerical simulations on receptivities of the Mach 4.5 boundary layer to free-stream fast acoustic waves at different incident wave angles. Specifically, 12 computational cases of different incident wave angles θ_∞ are considered, i.e.

Case number	1	2	3	4	5	6	7	8	9	10	11	12
θ_∞ (deg.)	0	7.5	15.0	18.0	20.0	22.5	30.0	37.5	45.0	60.0	75.0	90.0

All other flow conditions are the same for these cases. In particular, the frequencies of different cases are the same at $F = 2.2 \times 10^{-4}$. The adiabatic boundary condition is used for temperature perturbations on the wall for these cases. Equation (6) shows that the wavenumbers in the streamwise direction are different for cases of different incident wave angles. When θ_∞ increases, the horizontal components of the wavenumber k_x for the forcing fast acoustic waves decreases. For different incident wave angles, there always exist the components of fast acoustic waves propagating in the direction parallel to the wall surface owing to the diffraction and diffusion of transmitted acoustic waves inside the boundary layer near the leading edge. However, the amplitudes of the components for fast acoustic waves propagating in the direction parallel to the wall surface may change significantly with different incident wave angles. As discussed earlier, the excitation of mode I and mode II results from synchronization of fast acoustic waves propagating in the streamwise direction with these two modes. Therefore, the receptivity process in the boundary layer is expected to be strongly affected by the incident wave angles.

Figure 15 shows the wave amplitudes of pressure disturbances on the wall surface owing to planar free-stream fast acoustic waves for 4 of the 12 cases of different incident wave angles: $\theta_\infty = 0°, 22.5°, 45°$ and $75°$. As expected, the figure shows very

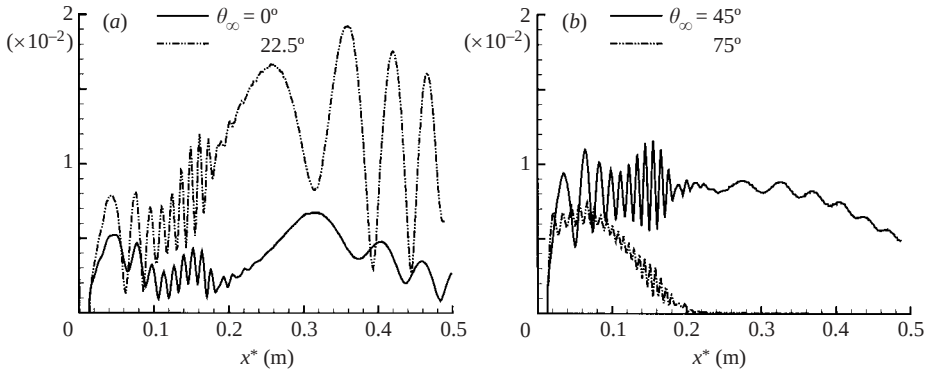

FIGURE 15. Amplitudes of pressure perturbations on the wall for the cases of free-stream fast acoustic waves at different incident wave angles ($F = 2.2 \times 10^{-4}$).

different wave amplitudes on the wall for cases of different incident wave angles. The common feature among these four cases is that there are strong wave modulations in pressure perturbations inside the second-mode region (0.1 m $< x^* <$ 0.2 m), which indicates the coexistence of several wave modes. As discussed earlier, the wave modulation in this region is a result of the interaction between the Stokes waves and the second Mack mode. In other words, the second-mode instability waves are always generated for all different incident acoustic wave angles. For cases of different incident wave angles, however, the induced second-mode wave amplitudes are different.

Figure 15 also shows very different amplitudes of mode II waves, which are excited in the region after the decay of the second mode. For the cases of $\theta_\infty = 0^\circ$ and $\theta_\infty = 22.5^\circ$, the second mode region is followed by a strong growth of mode II. As discussed earlier in this paper, the pressure perturbations on the wall are strongly amplified because of the resonant interaction between mode II waves and the fast acoustic waves in the region where the phase velocities of mode II waves and fast acoustic waves are close to each other. The peak value of mode II growth for the case of $\theta_\infty = 22.5^\circ$ reaches a very high value because of strong resonance. On the other hand, as θ_∞ increases further, the amplitudes of mode II decrease dramatically. For the case of $\theta_\infty = 75^\circ$, there are essentially no components of mode II in the mode II region. This is because horizontal components of fast acoustic waves, which result from diffusion and diffraction of incident transmitted fast acoustic waves inside the boundary layer, become very weak in the $\theta_\infty = 75^\circ$ case. As a result, the amplitudes of induced mode II waves by horizontal components of fast acoustic waves are too weak to be visible.

The receptivity characteristics of second mode, mode I and mode II can be measured by the response coefficients defined in (14). Figure 16 shows the response coefficients for computational cases of different incident acoustic wave angles. Each symbol in the plot represents one of the 12 computational cases of different incident wave angles with the same frequency. It shows that the receptivity of mode II has a much stronger receptivity response to the forcing fast acoustic waves than that of the unstable second mode. This is a significant result because it demonstrates the importance of stable modes in the receptivity process and shows the effects of incident wave angles on the receptivity process.

Figure 16 also shows that there is a dramatic change in the receptivity of mode I and mode II to planar free-stream fast acoustic waves with different incident wave

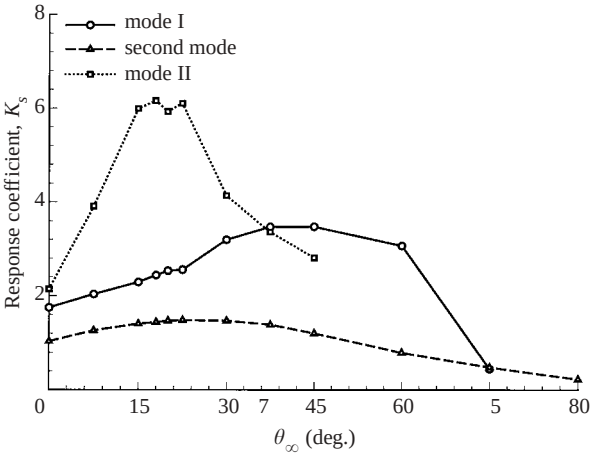

FIGURE 16. Response coefficients of the boundary-layer normal modes to free-stream acoustic waves *vs.* incident wave angles ($F = 2.2 \times 10^{-4}$).

angles. For a fixed frequency of the current case, there is an 'optimal' incident wave angle θ_∞ for each wave mode to reach maximum wave amplification. The maximum receptivity for mode II is reached for θ_∞ around 18°. The maximum receptivity for mode I is reached for θ_∞ around 45°. Compared with that of mode I and mode II, the response coefficient for the second mode is less sensitive to the change of the incident wave angles. The maximum receptivity for the second mode is reached for θ_∞ around 26°. The second mode is not very sensitive to the incident wave angles because the linear growth of the second mode is independent of the forcing waves. However, the second-mode waves are converted from mode I waves, which provide initial conditions for the second-mode waves and are affected by incident wave angles. Thus, the response coefficients of all discrete modes are affected by incident wave angles, although the sensitivities to this effect are different for different wave modes.

5.7. *Effect of forcing frequency*

In addition to the incident wave angles, the receptivity process is also strongly affected by the frequency of the forcing fast acoustic waves. To study the frequency effects on the receptivity process, the receptivity to the planar acoustic waves of four computational cases of different frequencies are studied. The four frequencies are: $F = 0.6 \times 10^{-4}$, 1.2×10^{-4}, 1.6×10^{-4} and 2.2×10^{-4}. Except for the frequencies, all four cases have the same flow conditions with zero incident wave angle for the forcing fast acoustic waves. The adiabatic boundary condition is used for temperature perturbations on the wall for these cases. Figure 17 shows the amplitudes of pressure perturbations on the wall generated by planar free-stream fast acoustic waves with zero incident wave angle and four different frequencies. From preceding analysis, different discrete boundary-layer normal modes and the Stokes waves with continuous spectra are generated inside the boundary layer by forcing fast acoustic waves. As a result, there are obvious oscillations in pressure amplitude curves owing to the modulation between different waves. Based on the results shown in Part 1 (figure 5), the existent region of the boundary-layer normal modes can be represented by the same range in terms of the dimensionless parameter RF for different frequencies. Consequently, as frequency F decreases, the existent region of normal modes in term of R will increase. In other words, all different mode existent regions expand with

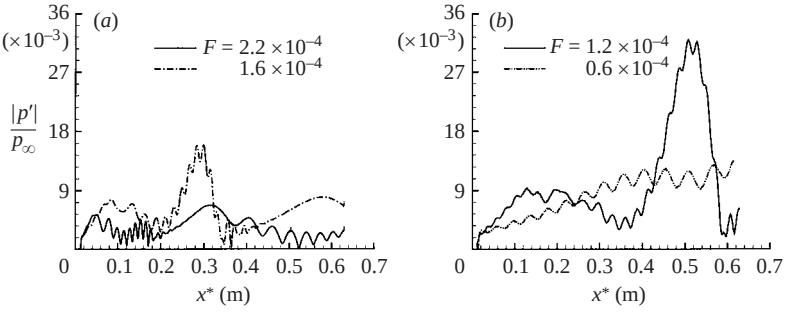

FIGURE 17. Amplitudes of pressure perturbations along the wall surface induced by free-stream fast acoustic waves of different frequencies ($\theta_\infty = 0°$).

decreasing frequency. The increase in R leads to the increase in the x-coordinate according to the following relation:

$$x^* = (\omega/F)^2/Re^*_\infty, \tag{15}$$

where $\omega = RF$. For fixed RF, $x^* \propto R^2 \propto F^{-2}$. Therefore, the generation locations of boundary-layer normal modes, such as mode II, and the second mode, will move downstream when F decreases. For example, the second-mode dominant region for the case of $F = 2.2 \times 10^{-4}$ is approximately in the range of $0.1\,\text{m} < x^* < 0.2\,\text{m}$, or $0.187 < RF < 0.264$. Based on (15), it is expected that the second-mode dominant regions will be $0.19\,\text{m} < x^* < 0.38\,\text{m}$, $0.34\,\text{m} < x^* < 0.67\,\text{m}$ and $1.34\,\text{m} < x^* < 2.69\,\text{m}$ for the other three cases of $F = 1.6\times10^{-4}$, 1.2×10^{-4} and 0.6×10^{-4}, respectively. Mode I waves are dominant upstream of the second-mode region, while mode II waves are dominant downstream of the second-mode region. Therefore, as the second-mode wave region moves downstream with decreasing F, the mode I wave region expands and the mode II wave region moves to further downstream, which is clearly shown in figure 17.

Unlike mode II and the second mode, mode I waves are always generated near the leading edge. However, the locations of peak amplitude for mode I waves move downstream when F decreases. At $F = 2.2 \times 10^{-4}$, mode I waves reach maximum amplitude at $x^* = 0.0492\,\text{m}$ or $RF = 0.131$. Similarly, the maximum amplitudes of mode I occur at $x^* = 0.084\,\text{m}$ (or $RF = 0.124$) and $0.144\,\text{m}$ (or $RF = 0.122$) for $F = 1.6 \times 10^{-4}$ and 1.2×10^{-4}, respectively. Again, the locations of induced maximum mode I waves in term of RF are almost the same for different frequencies. At $F = 0.6 \times 10^{-4}$, the maximum mode I amplitude occurs at the location outside the computational domain.

At $F = 1.6 \times 10^{-4}$, figure 17(a) shows that mode I is dominant near the leading edge ($0.0 < x^* < 0.20\,\text{m}$), while the second mode is dominant in the middle region ($0.20\,\text{m} < x^* < 0.38\,\text{m}$), followed by a mode II dominant region further downstream ($x^* > 0.38\,\text{m}$). The existent regions of the boundary-layer discrete modes are consistent with our expectation based on (15) and the results of the $F = 2.2 \times 10^{-4}$ case. Compared with the $F = 2.2 \times 10^{-4}$ case (figure 17a), the second-mode waves in the current case are more strongly amplified and become the dominant wave mode in the boundary-layer disturbances, while the peak of mode II does not change very much. As frequency decreases further to $F = 1.2 \times 10^{-4}$, pressure perturbations on the wall surface, shown in figure 17(b), are very similar in the growth pattern to that of the $F = 1.6 \times 10^{-4}$ case, with the exception that mode II waves will appear downstream

of the computational domain. Meanwhile, the second mode region moves further downstream, as expected. Again, the maximum amplitude of the second-mode wave is even higher compared with the $F = 1.6 \times 10^{-4}$ case. This result is expected based on the linear stability theory analysis of the frequency effect on the instability of the second mode. The growth of the second mode is due to its inherent unstable properties which can be predicted by the linear stability theory. The same growth rates curves *vs.* RF are obtained for the second mode at different frequencies in Part 1 (figure 17). Therefore, the second-mode waves are amplified more in the lower-frequency case. According to the linear stability theory, the second-mode Branch II neutral stability point is located at $RF = 0.2324$, or $x^* = 0.155$ m for frequency $F = 2.2 \times 10^{-4}$, or $x^* = 0.293$ m for frequency $F = 1.6 \times 10^{-4}$, or $x^* = 0.521$ m for frequency $F = 1.2 \times 10^{-4}$. Figure 17 shows that the second-mode waves reach the peak amplitudes at $x^* = 0.153$ m, 0.291 m and 0.510 m for $F = 2.2 \times 10^{-4}$, 1.6×10^{-4} and 1.2×10^{-4}, respectively. Therefore, the numerical solution and the LST results have very good agreement in the prediction of the Branch II neutral stability point for the second mode. For the last case of $F = 0.6 \times 10^{-4}$ (figure 17*b*), the expected second mode region ($1.34\,\text{m} < x^* < 2.69\,\text{m}$) is outside the computational domain. Therefore, only mode I waves and the Stokes waves are present in figure 17(*b*).

Similarly, the maximum mode II waves take place at $x^* = 0.312$ m (or $RF = 0.329$) for $F = 2.2 \times 10^{-4}$ and $x^* = 0.581$ m (or $RF = 0.327$) for $F = 1.6 \times 10^{-4}$. Again, for different frequencies, the locations of maximum mode II waves in term of RF are almost same.

Spatial Fourier analyses and band-pass filter windows are used to decompose the components of the second mode waves from the total boundary-layer disturbances. The response coefficients for mode I, the second mode and mode II are 2.32, 4.65 and 2.52, respectively, for the case of $F = 1.6 \times 10^{-4}$. The second mode is the most amplified among the three boundary-layer normal modes in this case. The response coefficients for mode I and the second mode are 2.94 and 9.88, respectively, for the case of frequency $F = 1.2 \times 10^{-4}$.

5.8. *Combined effects of incident wave angles and frequencies*

The boundary-layer receptivities to planar free-stream acoustic waves with different incident wave angles and different frequencies are also studied by numerical simulations. Specifically, three sets of incident wave angles are considered, i.e. $\theta_\infty = 0^\circ, 22.5^\circ$ and 45°. For each incident wave angle, three cases of different frequencies are simulated at $F = 1.2 \times 10^{-4}$, $F = 1.6 \times 10^{-4}$ and $F = 2.2 \times 10^{-4}$. Overall, there are nine computational cases with different combination of frequencies and incident wave angles. An adiabatic boundary condition is used for temperature perturbations on the wall for these cases. The response coefficients for mode I, mode II and the second mode are compared among these cases.

Figure 18 compares response coefficients for nine computational cases of different frequencies and incident wave angles. Owing to the exponential growth of the second mode, the response coefficients of the second mode are strongly affected by the change in wave frequencies. It shows that the response coefficients of the second mode are much larger for the cases of lower frequency with the same incident wave angle. On the other hand, for cases with the same frequency, the response coefficients for the second mode of the $\theta_\infty = 22.5^\circ$ case are larger than those of the other two cases of $\theta_\infty = 0^\circ$ and $\theta_\infty = 45^\circ$. Nevertheless, the effects of incident wave angles on the second-mode response coefficients are relatively weak compared to the effects of the frequencies.

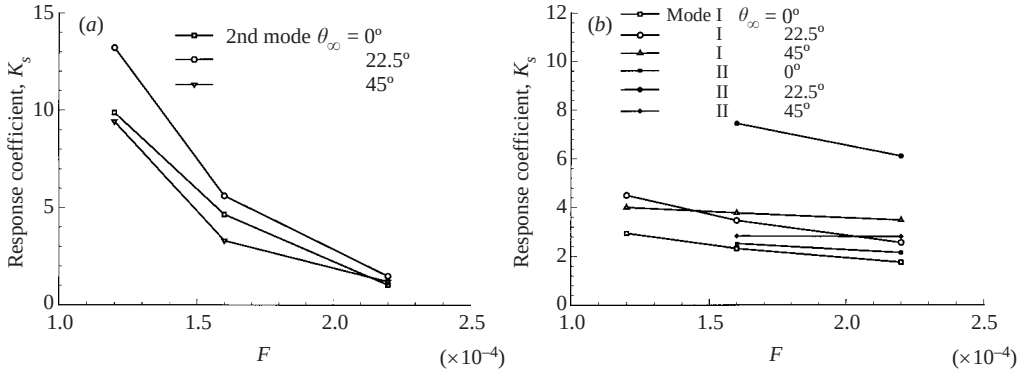

FIGURE 18. Response coefficients for cases of different frequencies and different incident wave angles.

The results for mode I and mode II are very different from those of the second mode in response to changing frequencies or incident wave angles. Figure 18 shows that the response coefficients of both mode I and mode II do not change very much when the frequencies change for cases of the same incident wave angle. As discussed earlier, this is because the amplifications of mode I and mode II are caused by a different mechanism from that of the second mode. Specifically, the growth of mode I and mode II results from their resonant interactions with the forcing fast acoustic waves, while the growth of the second mode is amplified owing to its inherent unstable property. As a result, the growth of mode I and mode II in the boundary layer is not sensitive to the change in frequencies, but very sensitive to the change in incident wave angles, while the growth of the second mode is not very sensitive to the change in incident wave angles, but very sensitive to the change in frequencies.

For cases of high frequencies ($F \geqslant 1.6 \times 10^{-4}$), the response coefficients of mode II may be larger than those of the second mode (when $\theta_\infty = 22.5°$, for example). As frequency decreases, the receptivity of the second mode increases substantially while the response coefficients of mode II stay about the same. Hence, the second mode response coefficients are much larger than those of mode II when $F \leqslant 1.2 \times 10^{-4}$. Among $\theta_\infty = 0°$, 22.5° and 45°, the maximum response coefficients of second mode and mode II take place at $\theta_\infty = 22.5°$. At $\theta_\infty = 22.5°$, the response coefficients based on the maximum pressure perturbations on the wall are 6.10 (mode II), 7.45 (mode II) and 13.2 (second mode) for $F = 2.2 \times 10^{-4}$, 1.6×10^{-4} and 1.2×10^{-4}, respectively.

5.9. *Branch I receptivity coefficient, K_I, of the second mode*

The objective of a receptivity study is to study the relationship between the induced boundary-layer instability waves and the free-stream forcing waves. For an incompressible boundary-layer flow over a flat plate, the receptivity can be measured by a Branch I receptivity coefficient (Saric *et al.* 2002) defined as the ratio of the induced T-S amplitude at the Branch I neutral stability location to the amplitude of free-stream disturbances, i.e.

$$K_I = \frac{|u'_{TS}|_I}{|u'_\infty|}, \tag{16}$$

where $|\cdot|$ stands for the amplitude values of the waves. The same definition can also be used to define a Branch I receptivity coefficient in a supersonic boundary layer. Since the second mode is the most important instability mode of interest in the current

Mach 4.5 supersonic boundary layer, only the Branch I receptivity coefficient for the second mode is considered in this paper.

In the current study of the receptivity of a supersonic boundary layer over a flat plate, the calculations of the Branch I receptivity coefficients from the simulation results are difficult because the complex transient flow fields contain many interacting wave modes. In this paper, the response coefficients of the second and other wave modes are used to characterize the responses of the wave modes to forcing disturbances. The response coefficients of the second mode, however, are influenced by both the initial receptivity process and the subsequent eigenmode growth in the region between the Branch I and Branch II neutral stability points. Consequently, the receptivity of the second mode is characterized better by the second-mode Branch I receptivity coefficient K_I defined by (16).

In order to compute the Branch I receptivity coefficient K_I for the second mode, it is necessary to determine the amplitude of the second mode at the branch I location. In our previous study on the characteristics of the boundary-layer normal modes by the DNS (figure 16 in Part 1), the amplitudes of the second-mode waves start to grow in our numerical simulations before they reach the Branch I neutral point predicted by the linear stability analysis. Therefore, it is difficult to locate the second-mode Branch I neutral stability point from the simulation results. On the other hand, the second-mode amplitudes at the Branch II location can be determined accurately from the numerical simulation results. Since the growth of the second mode from the Branch I to the Branch II locations is mainly caused by the eigenmode growth of the unstable second mode, the second-mode amplitude at the Branch I location can be determined by using the maximum wave amplitude at the Branch II location and an integration of the spatial growth rates between the Branch I and Branch II locations. Specifically, the amplitude rise from the Branch I to Branch II locations can be obtained by integrating the spatial growth rates obtained from the linear stability analysis with respect to x:

$$|p'|_{II} = |p'|_I \ \exp\left(\int_{x_I}^{x_{II}} -\alpha_i(\omega)\,\mathrm{d}x\right), \tag{17}$$

where $|p'|_I$ and $|p'|_{II}$ are the wave amplitudes at the Branch I (x_I) and Branch II (x_{II}) locations, respectively. From (17), the value of $|p'|_I$ can be determined from the value of $|p'|_{II}$ obtained by the numerical simulations and the integration of the growth rate α_i obtained by the linear stability analysis.

According to (17), for the cases of adiabatic wall boundary conditions, the amplitudes of the second-mode waves at the Branch II neutral points are 6.5, 13.3 and 27.0 times those at the Branch I neutral points for three cases of different frequencies at $F = 2.2\times10^{-4}$, 1.6×10^{-4} and 1.2×10^{-4}, respectively. Based on these amplitude ratio values, the second-mode Branch I receptivity coefficient K_I can be calculated from the second-mode response coefficients, which represent the ratio of maximum second-mode amplitude at the Branch II neutral point to the forcing acoustic wave amplitude. For the cases of adiabatic wall boundary conditions with $\theta_\infty = 0°$, the second-mode response coefficients are 1.03, 4.65 and 9.88 for $F = 2.2 \times 10^{-4}$, 1.6×10^{-4} and 1.2×10^{-4}, respectively. Therefore, the second-mode Branch I receptivity coefficients are calculated from the second-mode response coefficients to be:

$$F = 2.2 \times 10^{-4}, \qquad K_I = 0.158,$$
$$F = 1.6 \times 10^{-4}, \qquad K_I = 0.350,$$
$$F = 1.2 \times 10^{-4}, \qquad K_I = 0.366.$$

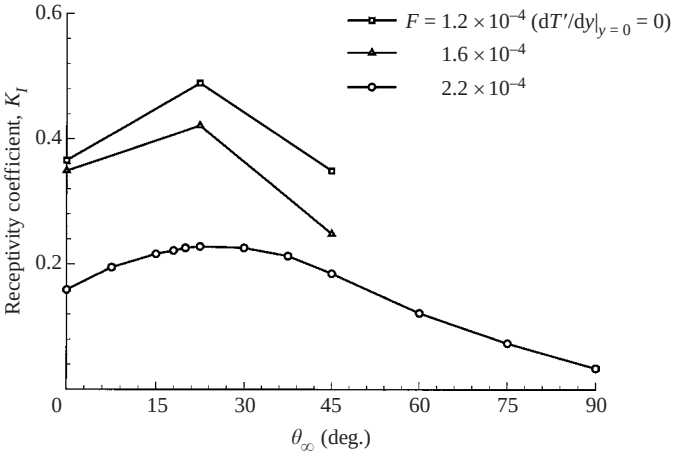

FIGURE 19. Branch I receptivity coefficients for cases of different frequencies and different incident wave angles.

The results show that the Branch I receptivity coefficients K_I increase when the frequencies of the forcing waves decrease.

Figure 19 shows the second-mode Branch I receptivity coefficients for the three cases of different frequencies as functions of the incident angles of the forcing acoustic waves. For a fixed frequency, the second-mode Branch I receptivity coefficients reach a maximum value at θ_∞ around 22.5°. Again, this figure shows that the second-mode Branch I receptivity coefficients increase when frequencies decrease. This is because the range of mode I waves is longer and the change of phase velocity of mode I waves is much slower at lower frequencies. The second mode waves are induced by the mode I waves, which are in turn induced by the forcing acoustic waves. At lower frequencies, the range of interaction between mode I waves and fast acoustic waves is longer. As a result, the induced mode I waves by the fast acoustic waves are stronger at lower frequencies. Since the second mode waves are induced by their interaction with the mode I waves, the initial amplitudes of the second-mode waves converted from mode I waves are stronger at lower frequencies, which leads to the increase of the second-mode Branch I receptivity coefficients at lower frequencies.

The second-mode Branch I receptivity coefficients can also be computed directly from the simulation results of the decomposed second-mode waves at Branch I neutral points predicted by the linear stability theory. For instance, at $F = 2.2 \times 10^{-4}$, the Branch I neutral point is predicted by the linear stability theory to be located at $x^* = 0.083\,\mathrm{m}$ ($R = 772.7$). The second-mode Branch I receptivity coefficient at this location for the case of $\theta_\infty = 0°$ can be calculated from figure 12 to be $K_I = 0.120$. This value is slightly lower than the value of $K_I = 0.158$ obtained by that of K_I computed by using the second-mode response coefficients (equation (17)). These two sets of values are different because it is difficult to determine accurately the second-mode wave amplitudes at the Branch I location as the second mode waves are very weak there. The weak second mode waves are mixed with other waves, and it is difficult to obtain a clean separation of the second mode from the simulation results by using the spatial Fourier analyses and band-pass filter windows without an aliasing effect, because the second mode is not dominant at the Branch I location. Therefore, the second-mode Branch I receptivity coefficient converted from the second-mode

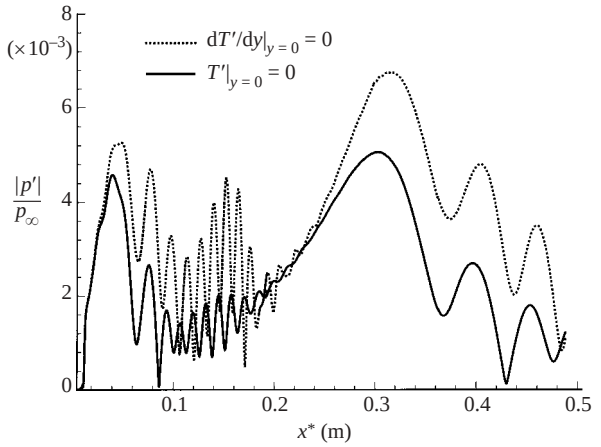

FIGURE 20. Pressure perturbation along the wall surface induced by free-stream fast acoustic waves of zero incident wave angle and different temperature boundary conditions ($F = 2.2 \times 10^{-4}$ and $\theta_\infty = 0°$).

response coefficient based on (17) is a better characterization of the second-mode receptivity than that obtained directly from the decomposed second-mode waves.

5.10. *Effect of wall temperature perturbation conditions*

In the current study, the steady base flow field is always the same supersonic boundary-layer flow over a flat plate with an adiabatic wall boundary condition. In the unsteady simulations, either adiabatic or isothermal conditions can be used for temperature perturbations on the wall. In practical applications, the temperature perturbation condition will be somewhere between these two extreme cases, so both boundary conditions have been considered in this paper. In this section, the effect of the wall temperature perturbation boundary conditions on the receptivity are investigated by numerical simulations.

To study the effect of wall temperature perturbation conditions on the boundary-layer receptivity properties, the receptivity to planar acoustic waves at fixed frequency $F = 2.2 \times 10^{-4}$ is considered. Both isothermal wall and adiabatic wall boundary conditions are used separately while all other flow conditions are the same. The forcing fast acoustic waves in the free-stream can impinge on the flat plate at different incident wave angles. The effects of incident wave angles on the receptivity have been discussed above by comparing 12 computational cases of different incident wave angles, and an adiabatic wall boundary condition has been used in these cases. Here, these cases are repeated and an isothermal wall boundary condition for temperature perturbations is used instead of an adiabatic wall boundary condition to investigate the effect of the wall temperature boundary condition on the receptivity.

Figure 20 compares the amplitudes of pressure perturbations induced by free-stream fast acoustic waves at $\theta_\infty = 0°$ for the two different wall boundary conditions of the temperature perturbations. The figure shows very similar wave patterns for both cases of different wall temperature boundary conditions. The main difference is that the amplitudes of pressure perturbations on the wall in the isothermal case are smaller than those in the adiabatic case, especially in the second mode region. A close examination of peak values of induced discrete boundary-layer normal modes in the figure shows that the second mode is much weaker for the isothermal case, while mode I and mode II are not affected very much by the change in the wall temperature

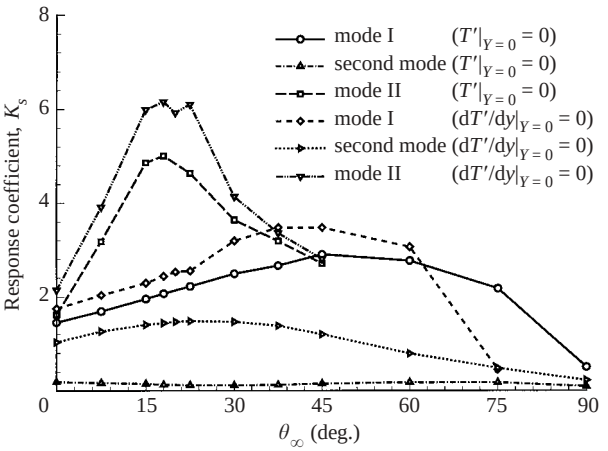

FIGURE 21. Comparison of receptivity of boundary-layer normal modes to planar free-stream acoustic waves with different incident wave angles and wall temperature boundary conditions ($F = 2.2 \times 10^{-4}$).

perturbation boundary conditions. Quantitatively, the response coefficients for the second mode, mode I and mode II in both the isothermal case and adiabatic case are:

	Isothermal case	Adiabatic case
Second mode:	$K_{second} = 0.187$	$K_{second} = 1.03$
Mode I:	$K_{modeI} = 1.45$	$K_{modeI} = 1.75$
Mode II:	$K_{modeII} = 1.62$	$K_{modeII} = 2.14$

It is obvious that the effect of temperature perturbation boundary conditions on receptivity of the second mode is different from that of mode I or mode II. Compared with the results for the isothermal case, the response coefficient of the second mode in the adiabatic case is 5.5 times larger. On the other hand, the response coefficients of mode I and mode II in the adiabatic case are only 1.2 and 1.3 times as large as those in the isothermal case. Therefore, because of the different receptivity mechanisms and stability properties among the second mode, mode I and mode II, the use of an isothermal wall boundary condition substantially stabilizes the second mode, but does not affect mode I and mode II very much.

Figure 21 compares response coefficients as a function of the incident wave angles for two groups of cases with two different wall boundary conditions for the temperature perturbations. The distributions of response coefficients for different incident wave angles are very similar for two groups of cases with different boundary conditions except that all response coefficients in the isothermal cases are smaller than corresponding values in the adiabatic cases. In particular, the response coefficients of the second mode are several times smaller for isothermal cases than those in adiabatic cases. On the other hand, the response coefficients for mode I and mode II of the isothermal cases are only moderately smaller than those of the adiabatic cases. The incident wave angle at which mode II reaches the maximum response coefficient is also about the same ($\theta_\infty = 18^\circ$) for the two groups of wall boundary conditions. The different effects on response coefficients for mode I (or mode II) and second mode are due to their different receptivity mechanisms.

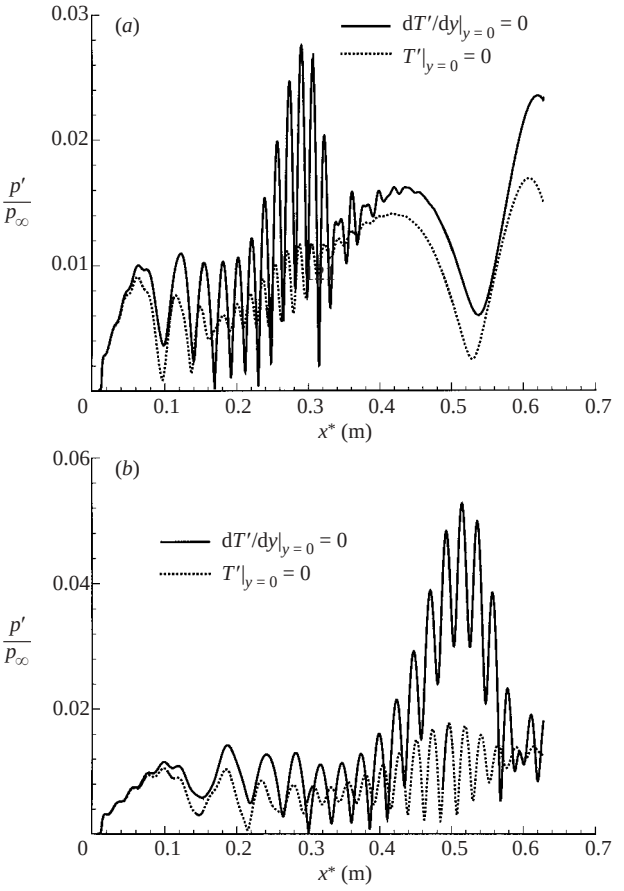

FIGURE 22. Pressure perturbation amplitudes along the wall surface induced by planar acoustic waves of different boundary conditions at two sets of different frequencies: (*a*) $F = 1.6 \times 10^{-4}$ and (*b*) $F = 1.2 \times 10^{-4}$ ($\theta_\infty = 22.5°$).

The general trend on the effects of wall temperature perturbation boundary conditions is also true for computational cases of other frequencies. Figure 22 shows the effect of different wall boundary conditions on the amplitudes of pressure perturbations along the wall surface owing to planar free-stream fast acoustic waves with an incident wave angle of $\theta_\infty = 22.5°$ at two different frequencies: (*a*) $F = 1.6 \times 10^{-4}$ and (*b*) $F = 1.2 \times 10^{-4}$. For both frequencies, pressure amplitudes are smaller in the isothermal cases than those in the adiabatic cases. For $F = 1.6 \times 10^{-4}$, the response coefficients of mode I, the second mode and mode II in the isothermal case and the adiabatic case are:

	Isothermal case	Adiabatic case
Second mode:	$K_{second} = 0.87$	$K_{second} = 5.61$
Mode I:	$K_{modeI} = 2.82$	$K_{modeI} = 3.47$
Mode II:	$K_{modeII} = 5.47$	$K_{modeII} = 7.45$

Again, the response coefficients of mode I and mode II in the isothermal case are relatively close to those in the adiabatic case. However, the response coefficient of the second mode in the adiabatic case is 8.56 times as large as that in the isothermal

case. As discussed earlier, for the cases of $F = 1.2 \times 10^{-4}$, mode II waves do not appear in the computational domain because the domain is not long enough. The response coefficients of mode I and the second mode of the isothermal case at this frequency are 3.19 and 2.44, respectively. The corresponding values of the adiabatic case are 4.50 and 13.2 for mode I and the second mode, respectively. The response coefficient of the second mode in the adiabatic case is 5.41 times as large as that in the isothermal case at $F = 1.2 \times 10^{-4}$.

There is a large difference in the response coefficients of the second mode between the adiabatic cases and the isothermal cases because the normal modes in the isothermal cases are linearly more stable than those of the adiabatic cases, which is shown in Part 1 (figure 10). Compared with adiabatic cases, mode I waves in isothermal cases are less amplified before they reach the peak values, which is clearly shown in figures 20 and 22. Furthermore, the amplitudes of mode I waves in the isothermal cases decay much faster and die down to a much smaller value when mode I waves propagate to the synchronization point between mode I and the first Mack mode. Then, mode I waves convert to Mack-mode waves. As a result, the initial amplitudes of the induced second Mack-mode waves by mode I waves are much smaller in the isothermal cases than those in the corresponding adiabatic cases. In addition, the growth rates of the second-mode waves are smaller for the isothermal case than those in the adiabatic cases. Therefore, the response coefficients of the second-mode waves are significantly smaller in the isothermal cases than those in the adiabatic cases. On the other hand, mode I and mode II are less affected by temperature perturbation boundary conditions because they are mainly induced by their resonant interactions with the forcing fast acoustic waves.

6. Receptivity to a beam of free-stream acoustic waves

In experiment, the free-stream disturbances may contain only a beam of fast acoustic waves other than continuous plane acoustic waves. In this section, receptivity to a beam of free-stream acoustic waves is studied by numerical simulations. Free-stream fast acoustic waves are allowed to enter the flow field through an incident slot on the shock boundary. The slot starts from $x_0^* = 0.01\,\mathrm{m}$ and ends at $x_1^* = 0.022\,\mathrm{m}$. The perturbation of free-stream acoustic waves satisfy (3)–(5) and the distribution of dimensionless amplitude ϵ is given by the following formula:

$$\epsilon = \epsilon_0 \left[\left(\frac{x^* - x_c^*}{(x_1^* - x_0^*)/2} \right)^2 - 1 \right]^2 \qquad \left(x_c^* - \tfrac{1}{2} l^* \leqslant x^* \leqslant x_c^* + \tfrac{1}{2} l^* \right), \quad (18)$$

where $\epsilon_0 = 5 \times 10^{-4}$, $l^* = 0.012\,\mathrm{m}$ and x_c^* is the coordinate of the centre of the incident slot. An adiabatic boundary condition is used for temperature perturbations on the wall in this section.

6.1. *A beam of acoustic waves with* $F = 2.2 \times 10^{-4}$ *and* $\theta_\infty = 0^\circ$

Figure 23 shows the contours of instantaneous pressure perturbations induced by a beam of free-stream fast acoustic waves with a frequency of $F = 2.2 \times 10^{-4}$ and an incident wave angle of $\theta_\infty = 0^\circ$. It shows that the forcing fast acoustic waves pass through an incident slot on the oblique shock. When transmitted fast acoustic waves propagate downstream, they penetrate the boundary layer and impinge on the wall between $x^* = 0.04\,\mathrm{m}$ and $x^* = 0.06\,\mathrm{m}$, which results in a number of reflected waves as

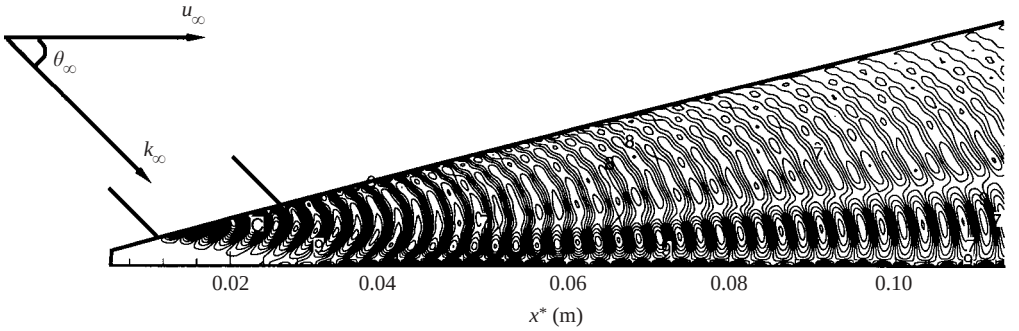

FIGURE 23. Contours of instantaneous pressure perturbations induced by a beam of free-stream fast acoustic waves ($F = 2.2 \times 10^{-4}$ and $\theta_\infty = 0°$).

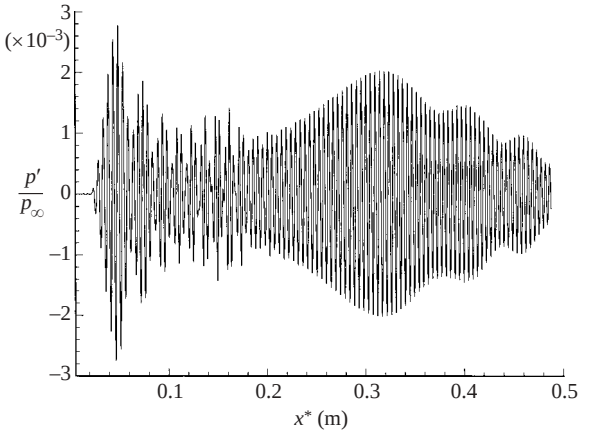

FIGURE 24. Instantaneous pressure perturbations along the wall surface induced by a beam of free stream fast acoustic waves entering the slot located at $x_c = 0.016\,\mathrm{m}$ ($F = 2.2 \times 10^{-4}$ and $\theta_\infty = 0°$).

well as boundary-layer disturbance waves including discrete normal modes and the Stokes waves.

Figure 24 shows the distribution of instantaneous pressure perturbations along the wall surface induced by a beam of free-stream fast acoustic waves. The first peak amplitude of pressure disturbances is due to the impingement of acoustic waves on the wall and the interaction between mode I waves and the acoustic waves. Then mode I waves convert to Mack-mode waves at the synchronization point ($x^* = 0.11\,\mathrm{m}$) between mode I and the Mack mode. The induced second Mack-mode waves are amplified when they enter the second-mode unstable region ($0.11\,\mathrm{m} < x^* < 0.155\,\mathrm{m}$). There is wave modulation between fast acoustic waves and the second-mode waves in this region. The second-mode waves decay and die down when they propagate further downstream. In the downstream region ($x^* > 0.2\,\mathrm{m}$), mode II waves are generated because of the synchronization between mode II waves and fast acoustic waves. Owing to the resonant interactions between mode II waves and acoustic waves, mode II waves are significantly amplified in this region. In the region even further downstream, mode II waves decay because of their inherent stable property.

Figure 25 shows the phase velocity distribution based on the pressure perturbations on the wall by using temporal Fourier analysis and (10) and (11). Again, the phase

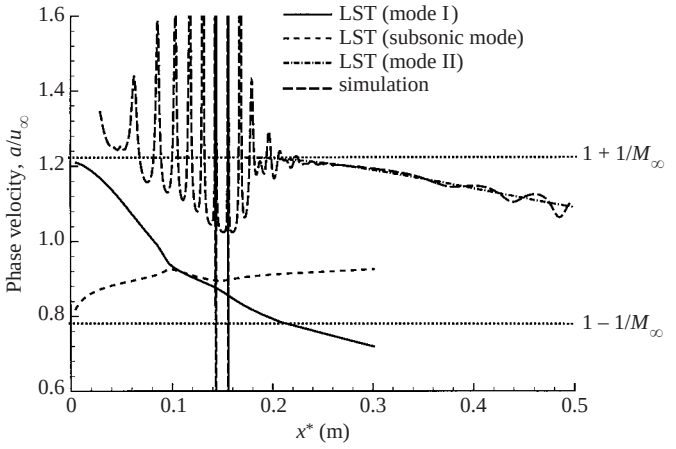

FIGURE 25. Distribution of phase velocities along the wall surface induced by a beam of acoustic waves entering the slot located at $x_c^* = 0.016\,\mathrm{m}$ ($F = 2.2 \times 10^{-4}$ and $\theta_\infty = 0°$).

velocities of the Mack modes, modes I and mode II from the linear stability theory are also plotted in the same figure for comparison with the numerical solutions. Unlike the phase velocities shown in figure 9 for boundary-layer disturbances induced by planar fast acoustic waves, boundary-layer disturbances induced by a beam of fast acoustic waves are strongly modulated by forcing fast acoustic waves. As a result, there are strong oscillations in the upstream phase velocity plot, shown in figure 25. In the region downstream ($x^* > 0.2\,\mathrm{m}$), the induced mode II waves are dominant. Therefore, the phase velocities from simulation agree with those of mode II predicted by the linear stability theory.

Spatial Fourier analyses and band-pass filter windows are used to decompose the second-mode waves from the total boundary-layer disturbances. For the current case of $\theta_\infty = 0°$, the response coefficients for mode I, the second mode and mode II are 0.875, 0.227 and 0.642, respectively.

6.2. *A beam of acoustic waves with different incident wave angles*

A beam of free-stream fast acoustic waves is allowed to enter the shock boundary with different incident wave angles to study the effects of incident wave angles on the boundary-layer receptivity. Four different incident wave angles, $\theta_\infty = 0°, 30°, 60°$ and $90°$, are considered. All other flow conditions are the same, i.e. $F = 2.2 \times 10^{-4}$ and the adiabatic wall condition is used for temperature perturbations.

The amplitudes of pressure perturbations on the wall induced by a beam of acoustic waves with frequency $F = 2.2 \times 10^{-4}$ and four different incident wave angles are shown in figure 26. It shows that the amplitudes of pressure perturbations reach peak values near the leading owing to the impingement of the forcing fast acoustic waves on the wall. Boundary-layer wave modes, such as mode I, mode II and the second mode, are generated afterwards. At $\theta_\infty = 90°$, the amplitudes of the induced second mode and mode II are too small to be visible. The effects of incident wave angles on receptivity will be discussed in the following subsection.

6.3. *Combined effects of incident wave angles and frequencies*

The effects of incident wave angles and frequencies on the boundary-layer receptivity to a beam of fast acoustic waves are studied by numerical simulations. At $F = 2.2 \times 10^{-4}$, thirteen computational cases of different incident wave angles evenly

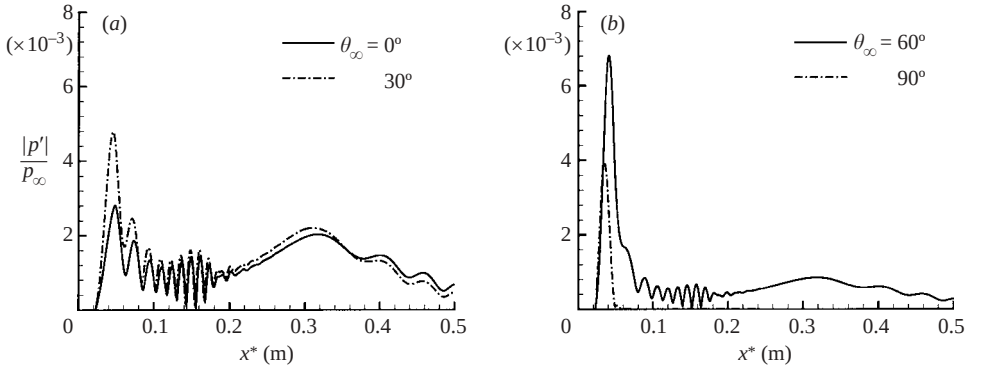

FIGURE 26. Amplitudes of pressure perturbations along the wall surface induced by a beam of free-stream fast acoustic waves entering the slot located at $x_c^* = 0.016\,\mathrm{m}$ with different angles ($F = 2.2 \times 10^{-4}$).

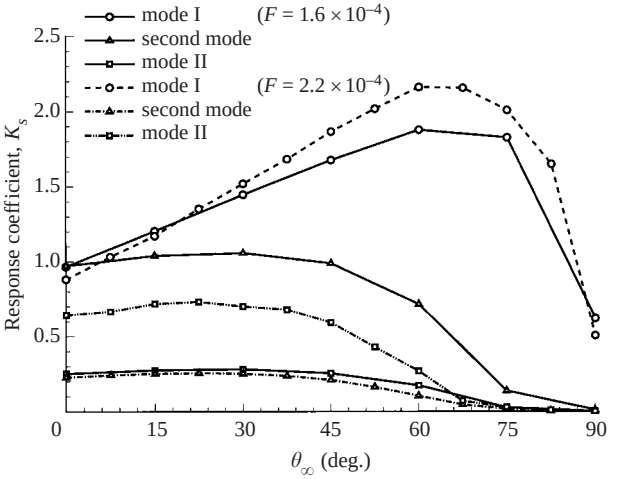

FIGURE 27. Response coefficients to a beam of free-stream acoustic waves *vs.* incident wave angles for two frequencies at $F = 2.2 \times 10^{-4}$ and $F = 1.6 \times 10^{-4}$.

spaced between 0° and 90° are considered. At $F = 1.6 \times 10^{-4}$, seven different incident wave angles evenly spanned between 0° and 90° are studied. At $F = 1.2 \times 10^{-4}$, three different incident wave angles, $\theta_\infty = 0°$, 22.5° and 45°, are considered. All other flow conditions are the same, and the adiabatic wall condition is used for temperature perturbations.

Figure 27 shows the response coefficients as functions of forcing incident wave angles for two group of cases with two different frequencies, i.e. $F = 2.2 \times 10^{-4}$ and $F = 1.6 \times 10^{-4}$. Again, the response coefficients of the second mode are not very sensitive to the incident wave angles when $\theta_\infty \leqslant 45°$, but response coefficients of mode I are very sensitive to the change in incident wave angles. For both groups of cases of different frequencies, the maximum response coefficients for mode I are obtained when the impingement wave angle θ_∞ is in the range of 60°–75°. For the second mode and mode II, the maximum response coefficients occur at θ_∞ around 22.5°.

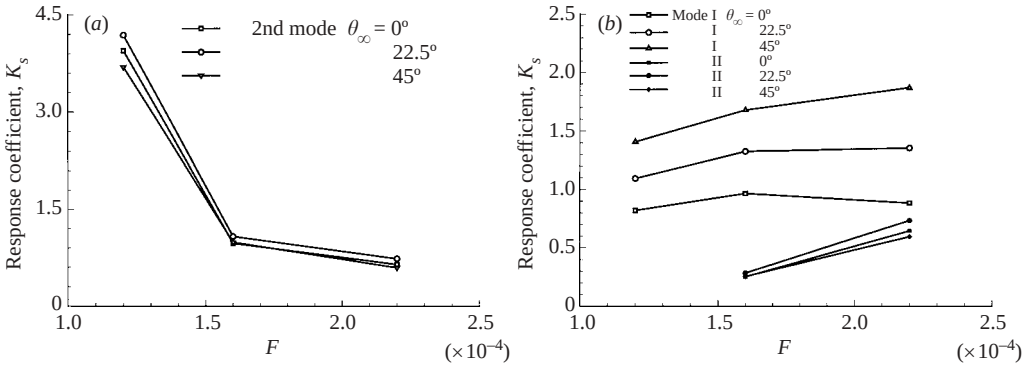

FIGURE 28. Response coefficients to a beam of free-stream fast acoustic waves at different frequencies and incident wave angles.

Figure 28 shows the response coefficients of boundary-layer normal modes to a beam of acoustic waves with different frequencies and incident wave angles. At $F = 1.2 \times 10^{-4}$, the receptivity of the second mode is dominant, while the receptivity of mode I is dominant for $F = 1.6 \times 10^{-4}$ and 2.2×10^{-4}. The response coefficients of the second mode increase significantly with decrease of frequencies. On the other hand, for the same incident wave angle, the response coefficients of mode II decrease when the frequencies decrease, which is in conflict with the results shown in figure 18. It is shown in figure 18 that the response coefficients of mode II increase when the frequencies decrease for receptivity to planar free-stream fast acoustic waves with the same incident wave angle. The conflict in effects of frequency on the response coefficients of mode II can be explained based on the receptivity mechanism of mode II. The generation and amplification of mode II waves are caused by synchronization and resonant interaction between mode II waves and fast acoustic waves. For receptivity to planar free-stream fast acoustic waves, there are continuous planar fast acoustic waves passing the shock and entering the boundary to provide perturbation energy for boundary-layer disturbances. Based on (15), the range of interaction between mode II waves and fast acoustic waves is longer for lower frequency. Therefore, the response coefficients of mode II increase as F decreases for receptivity to planar free-stream fast acoustic waves with fixed incident wave angle. However, for receptivity to a beam of free-stream fast acoustic waves, forcing disturbances can only enter the flow field through a narrow incident slot on the shock boundary. Downstream of the slot, there are no forcing acoustic waves passing the shock and entering the boundary layer to provide perturbation energy for boundary-layer disturbances. On the other hand, there is dissipation during propagation of the induced Stokes waves, which is dominated by fast acoustic waves. In other words, the amplitude of fast acoustic waves inside the boundary layer decay as they propagate downstream, which is shown in figure 29. Figure 29 shows the comparison of pressure perturbations on the wall induced by a beam of fast acoustic waves at the same incident wave angle $\theta_\infty = 0°$, but with two different frequencies, $F = 2.2 \times 10^{-4}$ and $F = 1.6 \times 10^{-4}$, respectively. It shows that the initial amplitude of mode II waves induced by fast acoustic waves at the beginning of the mode II region ($x^* = 0.2$ m for $F = 2.2 \times 10^{-4}$, and $x^* = 0.38$ m for $F = 1.6 \times 10^{-4}$) is much smaller for the $F = 1.6 \times 10^{-4}$ case, which indicates that the amplitudes of fast acoustic waves decay during propagation downstream. As a result, the interaction between mode II waves and fast acoustic waves becomes weaker for lower frequencies, although the range

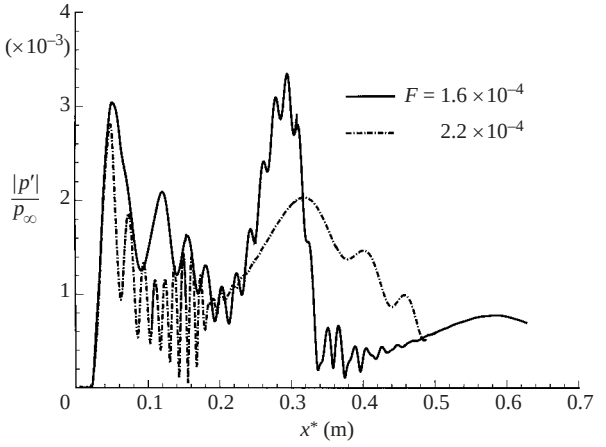

FIGURE 29. Comparison of pressure perturbations on the wall induced by a beam of free-stream fast acoustic waves at different frequencies ($\theta_\infty = 0°$).

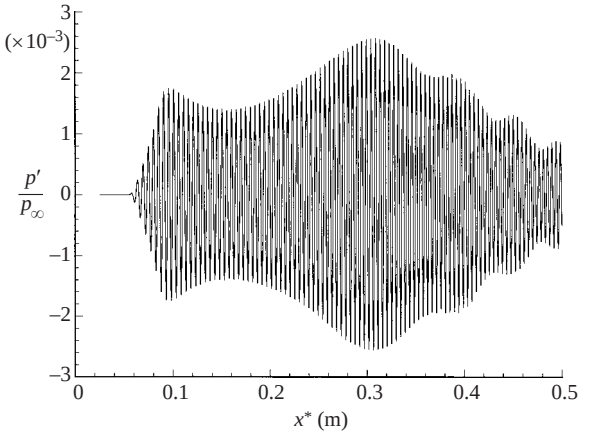

FIGURE 30. Instantaneous pressure perturbations along the wall surface due to a beam of free-stream fast acoustic waves entering the slot located at $x_c^* = 0.032\,\mathrm{m}$ ($F = 2.2 \times 10^{-4}$ and $\theta_\infty = 0°$).

of interaction is longer. Therefore, the response coefficients of mode II decrease as F decreases for receptivity to a beam of free-stream fast acoustic waves with fixed incident wave angle.

6.4. *Effect of incident slot locations*

To study the effect of incident slot locations on the boundary-layer receptivity, a number of cases are considered where a beam of forcing fast acoustic waves enter the oblique shock at different locations of incident slot.

Figure 30 shows the instantaneous pressure perturbations along the wall surface induced by a beam of acoustic waves at $\theta_\infty = 0°$ entering the incident slot spanning from $x^* = 0.026\,\mathrm{m}$ to $x^* = 0.038\,\mathrm{m}$ on the shock boundary. The first peak amplitude of pressure perturbations is due to the impingement and reflection of transmitted acoustic waves on the wall. This figure shows that induced wave components in the boundary layer consist mainly of mode II waves. However, the second mode does not appear in the flow field, which is different from the wave pattern shown in the

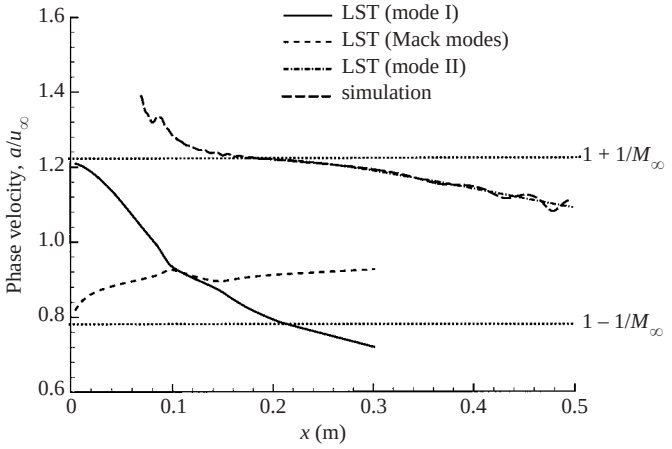

FIGURE 31. Distribution of phase velocities based on pressure perturbations on the wall for the case of a beam of free-stream fast acoustic waves entering the slot located at $x_c^* = 0.032\,\mathrm{m}$ ($F = 2.2 \times 10^{-4}$ and $\theta_\infty = 0°$).

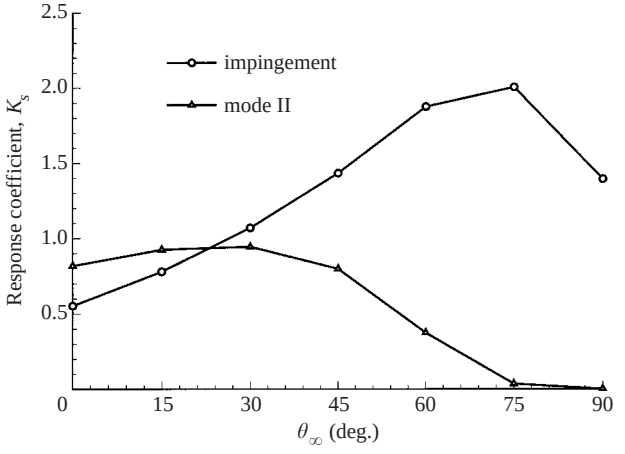

FIGURE 32. Response coefficients for a beam of acoustic waves with different incident wave angles ($F = 2.2 \times 10^{-4}$ and $x_c^* = 0.032\,\mathrm{m}$).

previous case (figure 24), where the incident slot is located closer to the leading edge than in the current case. Figure 31 compares the phase velocities between the results predicted by linear stability theory and those obtained by the numerical simulation. It is obvious that only mode II waves are generated in the current case. At the location of impingement, the phase velocity of mode I is much smaller than that of fast acoustic waves. Therefore, no mode I waves are generated by the forcing fast acoustic waves because there is no resonant interaction between mode I waves and fast acoustic waves. Consequently, no second-mode waves are generated in this case when mode I is absent, because the second mode is converted from mode I in the receptivity to fast acoustic waves.

The effects of incident wave angles on the receptivity of the current case are studied by considering a number of cases with different incident wave angles. Figure 32 shows the response coefficients measured at two peak amplitudes based on pressure

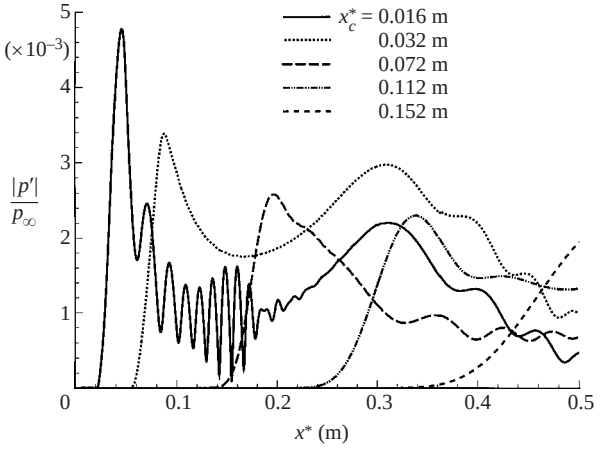

FIGURE 33. Comparison of the amplitudes of pressure perturbations along the wall surface for the case of a beam of free-stream fast acoustic waves entering the flow field through different locations ($F = 2.2 \times 10^{-4}$ and $\theta_\infty = 30°$).

perturbations on the wall. The first peak value is due to the impingement of acoustic waves on the wall, and the second peak value is due to the amplification of mode II. The maximum response coefficient is obtained from impingement at the acoustic angle $\theta_\infty = 75°$.

The effects of incident slot locations on receptivity to a beam of free-stream fast acoustic waves are also studied. A number of computational cases with fixed frequency of $F = 2.2 \times 10^{-4}$ and $\theta_\infty = 30°$ are considered, where the forcing wave incident slots are placed at different locations. The results of five cases of different incident slot locations are shown in figure 33. It shows that the impingement of the transmitted acoustic waves on the wall moves downstream when the centre of the incident slot is moved gradually from $x_c^* = 0.016$ m to $x_c^* = 0.152$ m. The location of the first peak value of pressure perturbation due to the impingement moves accordingly. The peak value of pressure perturbations decreases when the incident slot is moved downstream. Figure 33 also shows that when the impingement location of acoustic waves on the wall is close to the leading edge, the mode I, the second mode and mode II are generated in the boundary layer. As the location of the incident slot moves downstream, both mode I and the second mode are absent while mode II waves are amplified. As the impingement location moves even further downstream, mode I, the second mode and mode II are absent. These results again can be explained by the receptivity mechanisms of mode I, mode II, and the second mode. When the impingement location is close to the leading edge, mode I wave is synchronized with the forcing fast acoustic wave. As a result, mode I is generated in the boundary layer. Mode I then converts to the second mode. In the region further downstream, mode II is generated by resonant interaction with the forcing fast acoustic waves. As the forcing-wave impingement location moves downstream, mode I cannot be generated because the phase velocity of mode I is much smaller than that of fast acoustic waves at the location of impingement and there is no resonant interaction between mode I and fast acoustic waves. Therefore, only mode II is generated downstream. When the incident slot is moved from $x_c^* = 0.016$ m to $x_c^* = 0.032$ m, the induced mode II waves are more strongly amplified because there is less decay in fast acoustic waves and the resonant interactions between mode II waves and fast acoustic waves are stronger in

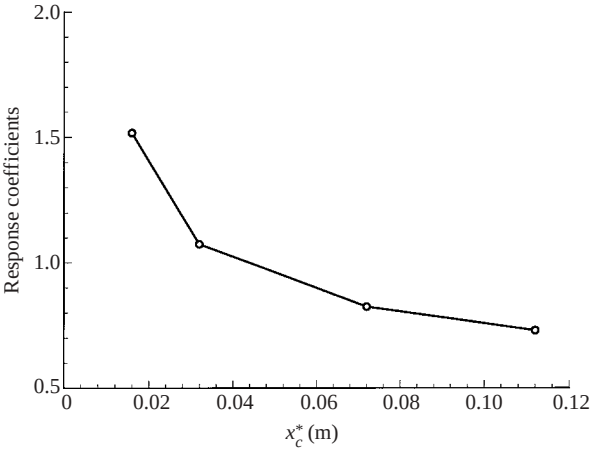

FIGURE 34. Response coefficients of boundary-layer disturbances due to impingement of a beam of free-stream fast acoustic waves with the incident wave angle at $\theta_\infty = 30^\circ$ entering the flow field through different locations ($F = 2.2 \times 10^{-4}$).

the latter case. However, when the incident slot is moved beyond $x_c = 0.072$ m, there are no amplified mode II waves shown in the boundary layer, because the phase velocity of mode II waves becomes much smaller than that of fast acoustic waves at the location of impingement and there are no resonant interactions between mode II waves and fast acoustic waves.

Figure 34 shows the maximum response coefficients of boundary-layer disturbances to a beam of acoustic waves at $\theta_\infty = 30^\circ$ entering the flow field through different incident slot locations. It is obvious that the response coefficients due to the impingement of acoustic waves on the wall are larger in the upstream region than those in the downstream region, which indicates that the leading edge is one of the most efficient regions for boundary-layer receptivity.

7. Results summary and conclusions

The receptivity of a Mach 4.5 supersonic boundary layer to free-stream fast acoustic waves is studied by numerical simulations in this paper. The receptivity properties are analysed based on numerical simulation results and linear stability analyses. The effects of incident wave angles, forcing wave frequencies, and wall temperature perturbations on the receptivity are studied.

7.1. *Mechanisms of boundary-layer receptivity to free-stream disturbances*

When fast acoustic waves are introduced from the free stream, the numerical results show that a number of wave modes are generated in the boundary layer by the receptivity process. The overall wave structures in the boundary layer induced by the forcing fast acoustic waves from the free stream are summarized below.

The receptivity of the flat-plate boundary layer to planar free-stream fast acoustic waves lead to the excitation and development of both Mack modes and the family of stable modes, i.e. mode I, mode II, etc. The generation of boundary-layer normal modes mainly results from the resonant interactions, which include interactions between the forcing fast acoustic waves and the stable modes (mode I, mode II, etc.) and those between the stable modes and the Mack modes (the first mode, the second mode, etc.). Specifically, the forcing fast acoustic waves from the free stream

first interact with the oblique shock and generate transmitted fast acoustic waves. The transmitted fast acoustic waves penetrate the boundary layer to form the Stokes waves which are the combination of fast acoustic waves, vorticity waves and entropy waves. Among the Stokes waves, the components of fast acoustic waves are dominant. The incident fast acoustic waves in the boundary layer are reflected by the wall surface after the impingement. As a result, mode I disturbances are first generated because the phase velocity of mode I near the leading edge is very close to that of the fast acoustic waves. The synchronization of the wavenumbers or wave speeds leads to a strong resonance between mode I waves and the fast acoustic waves. Though mode I is predicted to be stable by the linear stability theory, the amplitudes of the induced mode I waves grow as they propagate downstream because of the resonant interaction with the fast acoustic waves. After reaching the first peak value, mode I waves decay owing to their stable property after their phase velocities decrease during downstream propagation and there is no more resonance between mode I waves and fast acoustic waves.

Before mode I waves die out during propagation, they are synchronized with the Mack mode at their synchronization point, where both the first Mack mode and mode I have almost the same profiles of disturbance structure across the boundary layer. As a result, mode I waves convert to the Mack-mode waves in the synchronization region. Subsequently, the developed Mack-mode waves are amplified after they enter the second-mode unstable region. The second-mode waves decay after they pass the Branch II neutral stability point and become stable.

Meanwhile, in the region located approximately behind the second-mode unstable region, mode II waves are generated independently because of their synchronization with the fast acoustic waves. Because of the resonant interaction between mode II waves and the acoustic waves, mode II waves are significantly amplified even though mode II is predicted to be stable by the linear stability theory. Just like mode I waves, mode II waves decay owing to their stable property after their phase velocities decrease and there is no more resonance between mode II waves and the fast acoustic waves as they propagate downstream.

7.2. *Wave-mode decomposition and response/Branch-I-receptivity coefficients*

In the current receptivity study, the wavenumbers of the Mack modes, especially the second Mack mode, are considerably different from those of the acoustic waves. This fact is used to extract the wave components of the second Mack mode from the overall disturbance field in the boundary layer by means of a spatial Fourier analysis in order to quantitatively analyse the receptivity of the boundary layer to free-stream fast acoustic waves. The separated second mode structures are shown to agree well with those of the second mode predicted by the linear stability theory. The results of the separated second modes are used to compute both the response coefficients and the Branch I receptivity coefficients of the supersonic boundary layer.

Though the second mode waves can be separated from the total wave fields, it is impossible to decompose mode I (or mode II) and the acoustic waves from the total disturbances cleanly by using a band-pass filter window, because the wavenumbers of mode I (or mode II) are very close to those of the acoustic waves. Fortunately, the results indicate that, at the locations where mode I (or mode II) waves reach their maximum amplitudes, the wave components inside the boundary layer are dominated by the components for mode I (or mode II). This is evident in the comparison of wave structures of mode I and mode II from the linear stability theory with corresponding numerical solutions at those locations. Therefore, even though a clean

receptivity coefficient for mode I and mode II cannot be obtained from the numerical solutions, response coefficients can be obtained to serve as the approximate values of the receptivity coefficients by using the maximum wave amplitudes of mode I and mode II. Therefore, the response coefficients of the boundary layer are defined for both the Mack modes and the stable mode I and mode II to study the acoustic receptivity of the boundary layer quantitatively.

7.3. *Effects of incident wave angles, frequencies and wall temperature conditions*

The effects of incident wave angles on the receptivity are studied by considering planar free-stream fast acoustic waves at different incident wave angles. The excitation of mode I and mode II is a result of the synchronization between fast acoustic waves propagating in a streamwise direction and these two wave modes. The receptivities of mode I and mode II in the boundary layer are strongly affected by the incident wave angles of free-stream fast acoustic waves. The second mode, which is excited by mode I at their synchronization location, is not very sensitive to the change in incident wave angles because there is no direct interaction between the second-mode waves and forcing fast acoustic waves. However, for cases of different incident wave angles, the initial amplitudes of the second-mode waves are different because the second mode is induced by mode I, which is dependent on the incident wave angles. Thus, the receptivity of the second mode is also affected by the incident wave angles, although this effect is not as significant as that on mode I and mode II.

In addition to the incident wave angles, the receptivity process is also strongly affected by the frequencies of the forcing fast acoustic waves. The region of different wave modes for different frequencies can be represented by the same range in term of dimensionless parameter RF. Consequently, as frequency F decreases, the existent region of normal modes in terms of R will increases. Therefore, as the second-mode wave region moves downstream with decreasing F, the mode I wave region expands and the mode II wave region moves further downstream. The receptivity results for mode I and mode II are very different from those of the second mode in response to changing frequencies or incident wave angles. As frequency decreases, the existent regions of all different modes expand. Therefore, the second mode is amplified in a longer unstable region which leads to larger maximum amplitude of the second mode at the Branch II neutral point for lower frequencies. On the other hand, the response coefficients of both mode I and mode II do not change very much when the frequencies change for the same incident wave angle. The difference in the effects of frequency on receptivities of mode I, mode II and the second mode is because the amplifications of mode I and mode II result from different mechanisms from that of the second mode. Specifically, the growth of mode I and mode II result from the resonant interactions with the forcing fast acoustic waves, while the growth of the second mode is due to its inherent unstable property. As a result, the receptivity of mode I and mode II is not sensitive to the change in frequencies, but is very sensitive to the change in incident wave angles, while the receptivity of the second mode is not very sensitive to the change in incident wave angles, but is very sensitive to the change in frequencies.

The effect of the wall boundary condition for temperature perturbations on the receptivity to free-stream fast acoustic waves has also been investigated. The results of receptivity in both adiabatic cases and isothermal cases show very similar wave patterns inside the boundary layer. The main difference is that the response coefficients of the second mode are several times smaller in the isothermal cases than those in the adiabatic cases, while the receptivities of mode I and mode II are not affected very

much by the change in the wall temperature perturbation conditions. The different effects of the wall temperature perturbation conditions on receptivities of mode I (or mode II) and the second mode are due to the different receptivity mechanisms and stability properties of different boundary-layer normal modes. Specifically, mode I and mode II are less affected by temperature perturbation boundary conditions because they are generated and amplified by synchronization and resonant interaction with the forcing fast acoustic waves. Unlike mode I and mode II, the forcing fast acoustic waves do not interact directly with the second mode because of the large difference in phase velocities between the second-mode waves and fast acoustic waves. Instead, the second-mode waves are converted from mode I waves in receptivity to the fast acoustic waves. From the linear stability analysis, the normal modes in the isothermal cases are more stable than those in the adiabatic cases. Thus, the induced mode I waves in isothermal cases are less amplified than those in adiabatic cases. In addition, the amplitudes of mode I waves in the isothermal cases decay much faster and die down to a much smaller value when mode I waves convert to the Mack-mode waves at the synchronization point between mode I and the first Mack modes. As a result, the initial amplitudes of the induced second Mack-mode waves by mode I waves are much smaller in the isothermal cases than those in the corresponding adiabatic cases. Furthermore, the growth rates of the second mode are smaller in the isothermal case than those in the adiabatic case. Therefore, the receptivity coefficients of the second-mode waves are significantly smaller for the isothermal cases than those for the adiabatic cases.

7.4. *Receptivity to a beam of forcing fast acoustic waves*

The receptivity to a beam of fast free-stream acoustic waves with different frequencies and incident wave angles has also been investigated. To simulate the receptivity to a beam of free-stream acoustic waves, free-stream fast acoustic waves are allowed to enter the flow field through an incident slot on the shock boundary. The results show the same general trend in terms of the receptivity process for the case of a beam of acoustic waves as the previous cases of planar free-stream fast acoustic waves.

The effect of incident slot locations on the boundary-layer receptivity is studied by considering a number of cases where a beam of forcing fast acoustic waves enters the oblique shock at different locations. When the slot locations on the shock boundary change, the impingement locations of incident acoustic waves on the wall change accordingly. When the impingement location is close to the leading edge, mode I, the second mode and and mode II are generated sequentially in the boundary layer. As the location moves downstream, both mode I and the second mode are absent while mode II are amplified. As the impingement location moves even further downstream, mode I, the second mode and mode II are absent. These results can be explained by the receptivity mechanisms of mode I, mode II, and the second mode. The results also show that the response coefficients due to the impingement of acoustic waves on the wall are larger in the upstream region than in the downstream region. In other words, the leading edge is one of the most efficient regions for the boundary-layer receptivity.

7.5. *Conclusions*

The results of this paper show that the stable mode I waves play an important role in the receptivity process because they interact with both the forcing acoustic waves and Mack-mode waves. Through the interactions, mode I waves transfer perturbation energy from the forcing fast acoustic waves to the second Mack-mode waves. Mack-mode waves are induced by the mode I waves in receptivity to the free-stream fast

acoustic waves. Although both mode I and mode II are predicted to be stable by the linear stability theory, the induced mode I waves and mode II waves are strongly amplified owing to the resonant interactions with the forcing fast acoustic waves. At high frequencies, $F = 2.2 \times 10^{-4}$, for example, the receptivity of mode II, other than the second mode, may become the dominant component of boundary-layer disturbances. It is necessary to study receptivities of both unstable Mack modes and stable modes, such as mode I and mode II, in order to understand the receptivity process in the supersonic boundary layers.

Owing to different mechanisms of amplifications of mode I (or mode II) and the second mode, the effects of incident wave angles on the receptivity of mode I (or mode II) and the second mode are different. The receptivities of mode I and mode II are strongly affected by incident wave angles, but not sensitive to change in frequencies. On the other hand, the receptivity of the second mode is strongly affected by frequencies, but is not very sensitive to change in incident wave angles. For receptivity to the planar free-stream fast acoustic waves at fixed frequency $F = 2.2 \times 10^{-4}$, there is an 'optimal' incident wave angle θ_∞ for each wave mode to reach a maximum wave amplification. The maximum response coefficients of mode I, mode II and the second mode are obtained at $\theta_\infty = 45°$, $18°$ and $26°$, respectively. For the cases of adiabatic wall boundary conditions at $\theta_\infty = 0°$, the second-mode Branch I receptivity coefficient is $K_I = 0.158$ for the case of $F = 2.2 \times 10^{-4}$. The value of K_I increases when the frequencies of the forcing waves decrease.

Numerical simulations also show that the induced second mode by mode I is very weak in the isothermal cases. In addition, the induced second-mode waves are modulated by the Stokes waves inside the boundary layer. As a result, the growth of the second-mode waves affected by the Stokes waves becomes too weak to be detectable.

The results of receptivity to a beam of forcing fast acoustic waves provide further evidence that the second-mode waves are converted from mode I waves in the receptivity process. The response coefficients due to the impingement of acoustic waves on the wall are larger in the upstream region than in the downstream region, which indicates that the leading edge is one of the most efficient regions for boundary-layer receptivity.

This research was supported by the Air Force Office of Scientific Research, USAF, under AFOSR Grant F49620-00-1-0101. The program manager is Dr John Schmisseur. The views and conclusions contained herein are those of the authors and should not be interpreted as necessarily representing the official policies or endorsements either expressed or implied, of the Air Force Office of Scientific Research or the US Government.

REFERENCES

Arnal, D., Maslov, A. A., Sidorenko, A. & Shiplyuk, A. N. 1999 Experimental investigation of hypersonic boundary layer receptivity to acoustic disturbances. *Fluid Dyn.* **5**, 681–686.

Bayliss, A., Maestrello, L. & Krishnan, R. 1991 On the interaction between first and second-mode waves in a supersonic boundary layer. *Phys. Fluids* A **3**, 3014–3020.

Choudhari, M. & Strett, C. L. 1990 Boundary layer receptivity phenomena in three-dimensional and high-speed boundary layers. *AIAA Paper* 90–5258.

Choudhari, M. & Strett, C. L. 1993 Interaction of a high-speed boundary layer with unsteady free-stream disturbances. In *Transitional and Turbulent Compressible Flows* (ed. L. D. Kral & T. A. Zang), pp. 15–28. FED-151, ASME.

Fedorov, A. V. & Alexander, V. 1997 Laminar turbulent transition in a hypersonic boundary layer: receptivity and instability pre-history. *Final Rep.* NASA-N97-29589.

Fedorov, A. V. & Khokhlov, A. P. 1991 Excitation of unstable modes in a supersonic boundary layer by acoustic waves. *Fluid Dyn.* **4**, 67–74.

Fedorov, A. V. & Khokhlov, A. P. 1992 Sensitivity of a supersonic boundary layer to acoustic disturbances. *Fluid Dyn.* **1**, 40–47.

Fedorov, A. V. & Khokhlov, A. P. 2001 Prehistory of instability in a hypersonic boundary layer. *Theor. Comput. Fluid Dyn.* **14**, 359–375.

Fedorov, A. V. & Khokhlov, A. P. 2002 Receptivity of hypersonic boundary layer to wall disturbances. *Theor. Comput. Fluid Dyn.* **15**, 231–254.

Fedorov, A. V. & Tumin, A. 2001 Initial-value problem for hypersonic boundary layer flows. *AIAA Paper* 2001-2780.

Gaponov, S. A. 1977 Interaction of supersonic boundary layer with acoustic disturbances. *Fluid Dyn.* 51–56.

Goldstein, M. E. & Hultgren, L. S. 1989 Boundary-layer receptivity to long-wave free-stream disturbances. *Annu. Rev. Fluid Mech.* **21**, 137–166.

Guo, Y., Kleiser, L. & Adams, N. A. 1996 Comparison of Temporal and Spatial Direct Numerical Simulation of Compressible Boundary-Layer Transition. *AIAA J.* **34**, 683–690.

Kendall, J. M. 1967 Supersonic boundary-layer stability experiments. In *Proceedings of Transition Study Group Meeting* (ed. W. D. McCauley), 2(A), Aerospace Corp., San Bernardino.

Kendall, J. M. 1975 Wind Tunnel Experiments Relating to Supersonic and Hypersonic Boundary-Layer Transition. *AIAA J.* **13**, 290–299.

Kerschen, E. J. 1989 Boundary-Layer Receptivity. *AIAA Paper* 89-1109.

Kovasznay, L. S. G. 1953 Turbulence in Supersonic Flow. *J. Aero. Sci.* **20**, 657–682.

Ma, Y. & Zhong, X. 2003 Receptivity of a supersonic boundary layer over a flat plate. Part 1. Wave structures and interactions. *J. Fluid Mech.* **488**, 31–78.

Mack, L. M. 1975 Linear stability theory and the problem of supersonic boundary-layer transition. *AIAA J.* **13**, 278–289.

Mack, L. M. 1984 Boundary layer linear stability theory. In *AGARD Rep.* 709.

Malik, M. R. 1990 Numerical methods for hypersonic boundary-layer stability. *J. Comput. Phys.* **86**, 376–413.

Malik, M. R., Lin, R. & Sengupta, R. 1999 Computation of hypersonic boundary-layer response to external disturbances. *AIAA Paper* 99-0411.

Maslov, A. A. & Semionov, N. V. 1986 Excitation of nature oscillations in a boundary layer. *Fluid Dyn.* **3**, 74–78.

Maslov, A. A., Shiplyuk, A. N., Sidorenko, A. & Arnal D. 2001 Leading-edge receptivity of a hypersonic boundary layer on a flat plate. *J. Fluid Mech.* **426**, 73–94.

McKenzie, J. F. & Westphal, K. O. 1968 Interaction of linear waves with oblique shock waves. *Phys. Fluids* **11**, 2350–2362.

Pruett, C. D. & Chang, C. L. 1993 A comparison of PSE and DNS for high-speed boundary-layer flows. In *Transitional and Turbulent Compressible Flows* (ed. L. D. Kral & T. A. Zang), pp. 57–67. FED-151, ASME.

Saric, W. S., Reed, H. L. & Kerschen, E. J. 2002 Boundary-layer receptivity to freestream disturbances. *Annu. Rev. Fluid Mech.* **34**, 291–319.

Semionov, N. V., Kosinov, A. D. & Maslov, A. A. 1996 Experimental investigation of supersonic boundary-layer receptivity. In *Transitional Boundary Layers in Aeronautics* (ed. R. A. W. M. Henkes & J. L. van Ingen), pp. 413–420. North-Holland.

Semionov, N. V., Kosinov, A. D. & Maslov, A. A. 1998 An experimental study of instability disturbances excitation by external source in supersonic boundary layer of a blunt plate. In *Int. Conf. on the Methods of Aerophys. Res. (ICMAR'98), Novosibirsk, Russia*, pp. 192–197.

Zhong, X. 1998 High-order finite-difference schemes for numerical simulation of hypersonic boundary-layer transition. *J. Comput. Phys.* **144**, 662–709.

Zhong, X. 2001 Leading-edge receptivity to freestream disturbance waves for hypersonic flow over a parabola. *J. Fluid Mech.* **441**, 315–367.